Post-bifurcation and stability of a finitely strained hexagonal honeycomb subjected to equi-biaxial in-plane loading

Christelle Combescure, Pierre Henry, Ryan Elliott

CrossMark

Post-bifurcation and stability of a finitely strained hexagonal honeycomb subjected to equi-biaxial in-plane loading

Christelle Combescure [a,b], Pierre Henry [a,b], Ryan S. Elliott [a,*]

[a] *Department of Aerospace Engineering and Mechanics, University of Minnesota, Minneapolis, MN 55455, USA*
[b] *Laboratoire de Mecanique des Solides (CNRS UMR 7649), Ecole Polytechnique, Route de Saclay, 91128 Palaiseau, France*

A B S T R A C T

The buckling and crushing mechanics of cellular honeycomb materials is an important engineering problem. Motivated by the pioneering experimental and numerical studies of Papka and Kyriakides (1994, 1999a,b), we review the literature on finitely strained honeycombs subjected to in-plane loading and identify two open questions: (i) How does the mechanical response of the honeycomb depend on the applied loading device? and (ii) What can the *Bloch wave representation* of all bounded perturbations contribute to our understanding of the stability of post-bifurcated equilibrium configurations? To address these issues we model the honeycomb as a two-dimensional infinite perfect periodic medium. We use analytical group theory methods (as opposed to the more common, but less robust, imperfection method) to study the honeycomb's bifurcation behavior under three different far-field loadings that produce (initially) the same equi-biaxial contractive dilatation. Using an FEM discretization of the honeycomb walls (struts), we solve the equilibrium equations to find the principal and bifurcated equilibrium paths for each of the three loading cases. We evaluate the structure's stability using two criteria: *rank-one convexity* of the homogenized continuum (long wavelength perturbations) and Bloch wave stability (bounded perturbations of arbitrary wavelength). We find that the post-bifurcation behavior is extremely sensitive to the applied loading device, in spite of a common principal solution. We confirm that the *flower mode* is always unstable, as previously reported. However, our (first ever) Bloch wave stability analysis of the post-bifurcated equilibrium paths shows that the flower mode is stable for all sufficiently short wavelength perturbations. This new result provides a realistic explanation for why this mode has been observed in the finite size specimen experiments of Papka and Kyriakides (1999a).

© 2016 Elsevier Ltd. All rights reserved.

1. Introduction

The buckling and crushing mechanics of cellular honeycomb materials subjected to in-plane loading has been a long-standing problem of practical importance to the engineering community, primarily due to their wide use in shock absorption and mitigation. The theoretical interest in this problem stems from the fact that it represents a prototypical example of nonlinear mechanical systems exhibiting instabilities that lead to strain localization and quasi-static propagating *shear-bands*. The excellent monograph by Gibson and Ashby (1997), now in its second edition, provides a thorough presentation, from the materials science viewpoint, of what is known about the behavior of such materials.

From the wide literature on the subject, the review of which is beyond the scope of this work, attention is focused here on the two-dimensional problem of in-plane crushing of honeycombs. Detailed studies have appeared on this topic in the mechanics literature, both experimental (Papka and Kyriakides, 1994, 1998, 1999a; 1999b, among others) and theoretical (Ohno et al., 2002; Okumura et al., 2002; Saiki et al., 2005, 2002; Triantafyllidis and Schraad, 1998). However, many open questions remain about the particular mechanisms by which honeycomb materials progressively buckle in a sequence that ultimately makes up their highly complex mechanical response to in-plane loading. Moreover, there seems to be some ambiguity in the literature regarding the application and effect of different mechanical loading devices as well as ambiguity in regard to the stability of the bifurcated equilibrium paths.

In this paper, we first review the relevant literature with a focus on the onset of instability, initial post-bifurcation and the stability of the resulting bifurcated equilibrium paths in finitely strained cellular solids with hexagonal symmetry under different in-plane loading conditions. Next, we investigate the behavior of an infinite, perfect, two-dimensional hexagonal honeycomb subjected to equi-biaxial compression from multiple loading devices. We use

---

analytical symmetry group theory methods (as opposed to the more common, but less robust, imperfection method) to study the honeycomb's bifurcation behavior under three different far-field loading conditions that produce (initially) the same equi-biaxial contractive dilatation: displacement control, dead load Biot stress control, and live load pressure control. Using the primitive unit cell (smallest possible periodic domain) and an FEM discretization of the honeycomb walls (struts), we solve the associated equilibrium equations, identify the principal path and bifurcation points along this path. Each bifurcation point corresponds to a loss of symmetry (either rotational, translational, or both) along the bifurcating equilibrium paths and group theory methods identify an appropriate primitive unit cell for each such path. Using the appropriate unit cell and the corresponding FEM mesh, we solve the associated equilibrium equations and compute the post-bifurcation behavior for the honeycomb in each of the three loading cases. For all obtained equilibrium configurations, we evaluate the structure's stability using two criteria: *rank-one convexity* of the homogenized continuum (for long wavelength perturbations) and Bloch wave stability (for bounded perturbations of arbitrary wavelength).

The presentation is organized as follows: in Section 2 we review the recent literature on the theoretical and numerical modeling of instability and bifurcation of honeycombs subjected to in-plane loading. In Section 3 we describe our theoretical and numerical model of a perfect, infinite, two-dimensional hexagonal honeycomb structure and the various loading devices considered. In Section 4 we present the equilibrium and stability problem of interest and discuss the symmetry-based branch-following and bifurcation techniques employed in the numerical (FEM based) solution of the nonlinear equilibrium equations. In Section 5 we report the results obtained from our simulations, and finally in Section 6 we conclude with a critical discussion and perspectives on the obtained results.

2. Previous investigations of the in-plane loading of honeycombs

The study of cellular solids has been a major topic of research in mechanics over the past few decades. However the analysis of the stability and post-bifurcation behavior of regular honeycomb structures has only been addressed relatively recently. The following is a short bibliographic review of papers which are relevant to the current study.

2.1. Experimental characterization

The investigation by Papka and Kyriakides (1994) on the uniaxial in-plane crushing of hexagonal aluminum honeycomb was the first in-depth study on this topic from the mechanics standpoint. These authors established the link between a bifurcation on the principal solution and the onset of localization due to the subcritical nature of the post-bifurcated equilibrium path (i.e. a reduction in load carrying capacity of the structure with increasing bifurcation amplitude). They also showed how the repetition of the above mechanism explains the sequential crushing of the cell rows, leading to the plateau behavior in the load–deformation response, which is the most characteristic (and technologically useful) aspect of the nonlinear behavior of these materials.

The subsequent work of Papka and Kyriakides (1999a) is an experimental study of the biaxial crushing of circular cell honeycombs and provides one of the best available accounts of the biaxial, in-plane loading behavior of hexagonal honeycomb materials. The authors use a custom made testing facility to crush polycarbonate honeycomb specimens of size 18×21 unit cells, investigating several bi-axiality ratios. The experiments aim to apply affine

displacement-control boundary conditions to the specimen[1]:

$$\mathbf{x} = \mathbf{FX}, \forall \mathbf{X} \in \partial \Omega, \tag{1}$$

where Ω is the body of the specimen, $\partial \Omega$ its boundary, and

$$\mathbf{F} = \begin{bmatrix} F_{xx} & 0 \\ 0 & F_{yy} \end{bmatrix}, \tag{2}$$

is the form of the deformation gradient (with respect to a Cartesian coordinate system aligned with the frame of the testing facility) used to describe the affine boundary conditions that the facility is capable of prescribing. Figs. 1 and 2 show the deformation sequence of the honeycomb material under equi-biaxial compression ($F_{xx} = F_{yy} < 1$). The initial response of the honeycomb is elastic up to the onset of instability where a *flower-like* mode develops. Much of the specimen behaves like the cluster of cells shown in Fig. 2, with a rather undeformed central cell and six surrounding highly deformed cells. This regular pattern is broken up in several places, due to a combination of three factors: edge effects, friction at the sliding boundary conditions and incompatibility of the mode of deformation with a finite specimen.

Figs. 3 and 4 show the deformation sequence of the honeycomb material with $F_{yy}/F_{xx} = 2$. The behavior of the honeycombs under these loading conditions is similar to the equi-biaxial compression. At the onset of instability, an almost flower-like mode develops. This mode is similar to the equi-biaxial flower-like mode but now the hexagonal C_6 symmetry of the mode is broken causing the entire flower-like pattern to experience a uniform deviation aligned with the principal axes of the applied affine boundary conditions. The pattern is not as uniform throughout the specimen as in the case of equi-biaxial compression, and the final collapse of the specimen spreads from these localized high-deformation regions.

Fig. 5 shows the localized deformation sequence of the honeycomb material with $F_{yy}/F_{xx} = 3$. Here the behavior is similar to that when $F_{yy}/F_{xx} = 2$, except that now a competing *rectangular* mode is observed in some regions of the specimen.

The experiments of Papka and Kyriakides (1999a) show that the in-plane biaxial crushing of circular cell honeycomb materials is a complex mechanical process involving an initial loss of stability associated with a flower-like or rectangular deformation mode followed by strain localization and propagation and finishing with densification of the material. These experimental results (as well as their previous work, Papka and Kyriakides, 1994; 1998) have inspired a number of theoretical studies that aim to explain the observed behavior associated with the onset of instability in such materials. These theoretical studies are reviewed next.

2.2. Characterization of the onset of failure

The paper by Triantafyllidis and Schraad (1998) performs a semi-analytical study of the onset of failure for infinite two-dimensional hexagonal cell honeycomb materials subjected to a

---

[1] In this paper we use the direct tensor notation of Tadmor et al. (2012). In this notation $\mathbf{x} = \mathbf{FX}$ has the indicial form $x_i = F_{iJ}X_J$ (where summation on repeated indices is implied) and represents the contracted multiplication operation. A tensor product of a second-order tensor and a first-order tensor (vector) is denoted $\mathbf{T} \otimes \mathbf{a}$ with indicial form $T_{ij}a_k$. A centered dot between two vectors, as in $\mathbf{a} \cdot \mathbf{b}$, represents the inner product. Thus, the fully contracted product of a second-order tensor is written $\mathbf{a} \cdot (\mathbf{Tb})$ with indicial form $T_{ij}a_ib_j$. A double dot represents the inner product on second-order tensors, as in $\mathbf{T} : \mathbf{S}$ and has the indicial form $T_{ij}S_{ij}$. This notation is also extended to the fully contracted product of a fourth-order tensor $\mathbf{T} : \mathbf{K} : \mathbf{S}$ with indicial form $T_{ij}K_{ijkl}S_{kl}$.

Fig. 1. Sequence of deformed configurations of honeycomb material subjected to equi-biaxial ($F_{xx} = F_{yy}$) loading conditions. From Papka and Kyriakides (1999a) with permission.

Fig. 2. Deformation patterns of a cluster of cells subjected to equi-biaxial ($F_{xx} = F_{yy}$) loading conditions. From Papka and Kyriakides (1999a) with permission.
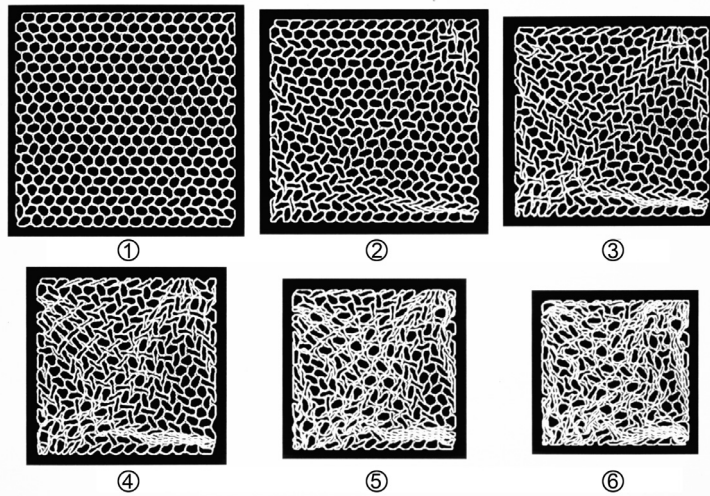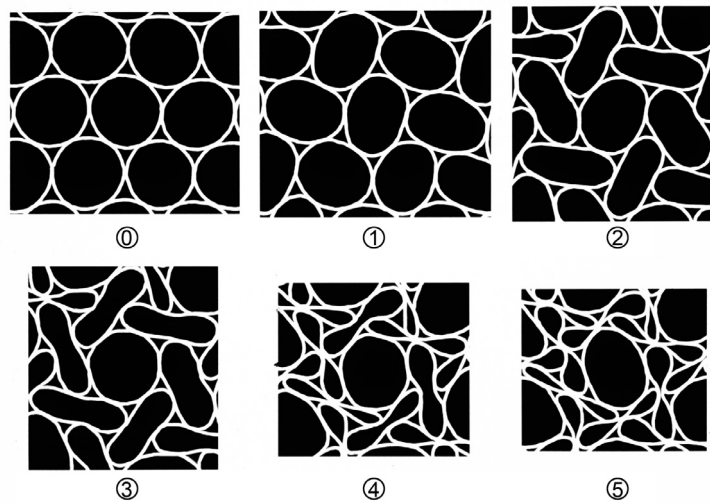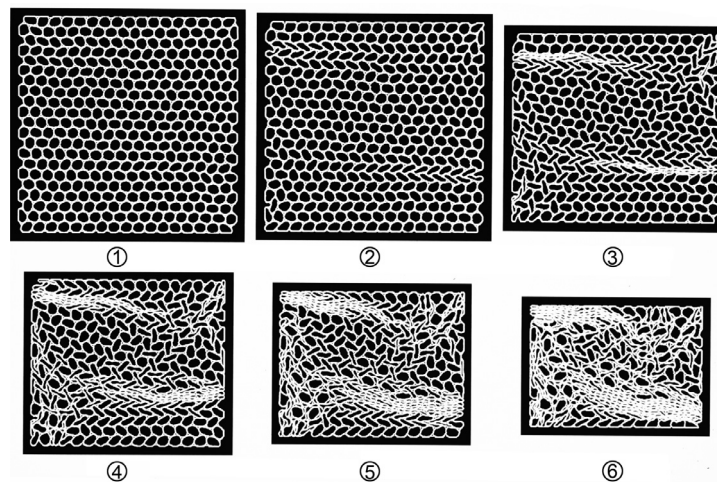

Fig. 3. Sequence of deformed configurations of the honeycomb material subjected to biaxial $F_{yy}/F_{xx} = 2$ loading conditions. From Papka and Kyriakides (1999a) with permission.
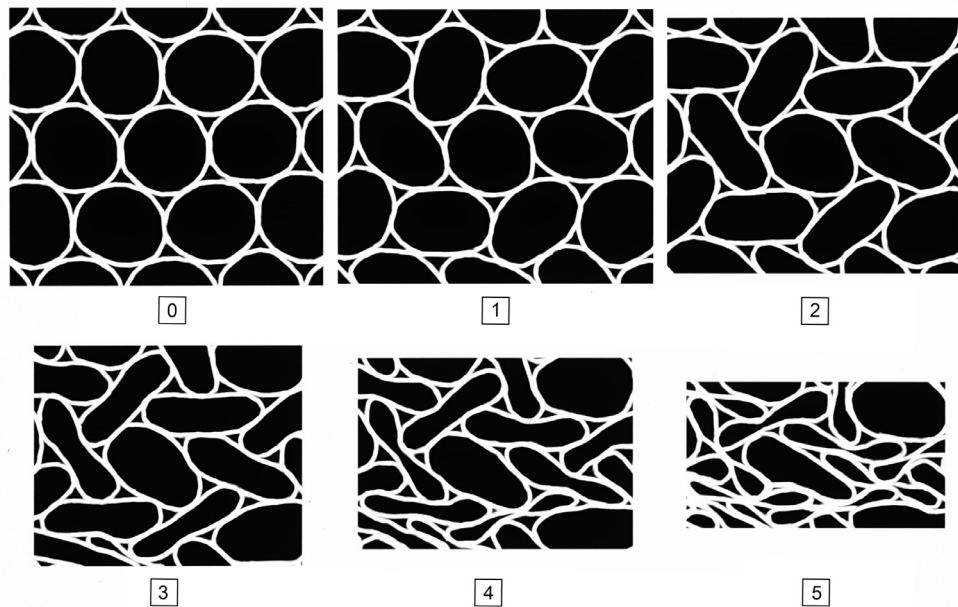
Fig. 4. Deformation patterns of a cluster of cells subjected to biaxial $F_{yy}/F_{xx} = 2$ loading conditions. From Papka and Kyriakides (1999a) with permission.

Fig. 5. Deformation patterns of a cluster of cells subjected to biaxial $F_{yy}/F_{xx} = 3$ loading conditions. From Papka and Kyriakides (1999a) with permission.
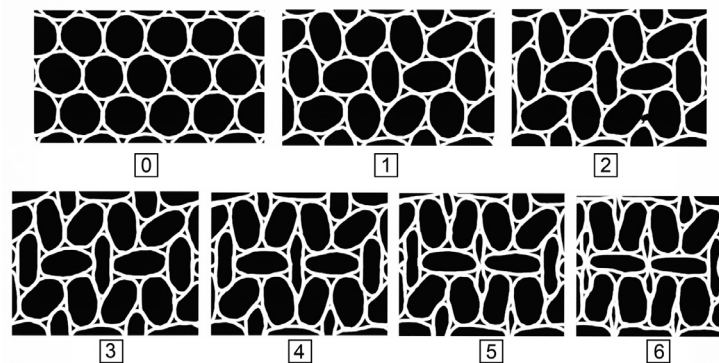
far-field compressive first Piola–Kirchhoff stress of the form

$$\mathbf{\Pi} = \frac{1}{A_1 A_2} \begin{bmatrix} \cos\theta & -\sin\theta \\ \sin\theta & \cos\theta \end{bmatrix} \begin{bmatrix} \Lambda\cos\phi & 0 \\ 0 & \Lambda\sin\phi \end{bmatrix}$$
$$\times \begin{bmatrix} \cos\theta & \sin\theta \\ -\sin\theta & \cos\theta \end{bmatrix}, \qquad (3)$$

given with respect to a Cartesian coordinate frame aligned with the symmetry axes of the honeycomb consistent with that used by Papka and Kyriakides (1999a). Here, A_1 and A_2 are the unit cell side lengths (as given in Fig. 6), Λ is the amplitude of loading, θ is the orientation angle of the principal stress axes and ϕ describes the biaxial nature of the applied dead loading. Proportional loading (fixed values of ϕ and θ) paths are considered, for which a non-dimensional displacement Δ/h (where h is the out-of-plane thickness of the honeycomb), work-conjugate to the applied loading, can be defined. In order to better model real honeycomb materials the vertical hexagonal cell walls have twice the thickness of the others. The honeycomb material itself is modeled using a fully nonlinear (large displacement and large rotation) beam model and a linearly-elastic/linearly-plastic constitutive model. The unit cell chosen to represent the infinite periodic system is shown in Fig. 6, and periodic boundary conditions are enforced.

Using this model of the infinite honeycomb material the authors investigate the *onset of failure* (defined as the first occurrence

of loss of local uniqueness of the principal equilibrium path) along every possible proportional loading path. The onset of failure can occur due to the occurrence of a bifurcation point, a maximum-load point, or the onset of plasticity along the principal equilibrium path. Note that this definition of *onset of failure* does not necessarily coincide with the principal equilibrium path's *onset of instability*.

The authors apply a semi-analytical technique combining the theory of Bloch waves and a finite-element model of the honeycomb unit cell, to establish the theoretical failure surface of the perfect infinite honeycomb.[2] They also investigate geometric scale effects and imperfection effects on the failure surfaces.

---

[2] The stability of Bloch waves has been identified as an important measure of stability for microstructured materials since, at least, the pioneering 1993 work of Geymonat et al. (1993). Indeed, these ideas have been extensively employed ever since by Triantafyllidis and co-workers (Dobson et al., 2007, 2006; Elliott, 2007; Elliott et al., 2006a, 2006b, 2011; Gong et al., 2005; Jusuf, 2013; Michailidis et al., 2009; Michel et al., 2007; Sorkin et al., 2014; Triantafyllidis and Schraad, 1998) and they are starting to propagate into the current applied literature as well (Laroussi et al., 2002; Liu and Bertoldi, 2015). There is also a history of recognition that bifurcating equilibrium branches that are described by Bloch waves exist in many physical problems with spatial periodicity. For example, in the nonlinear Schrödinger equation where work on these ideas has existed since at least the early 1990s (Heinz et al., 1992).
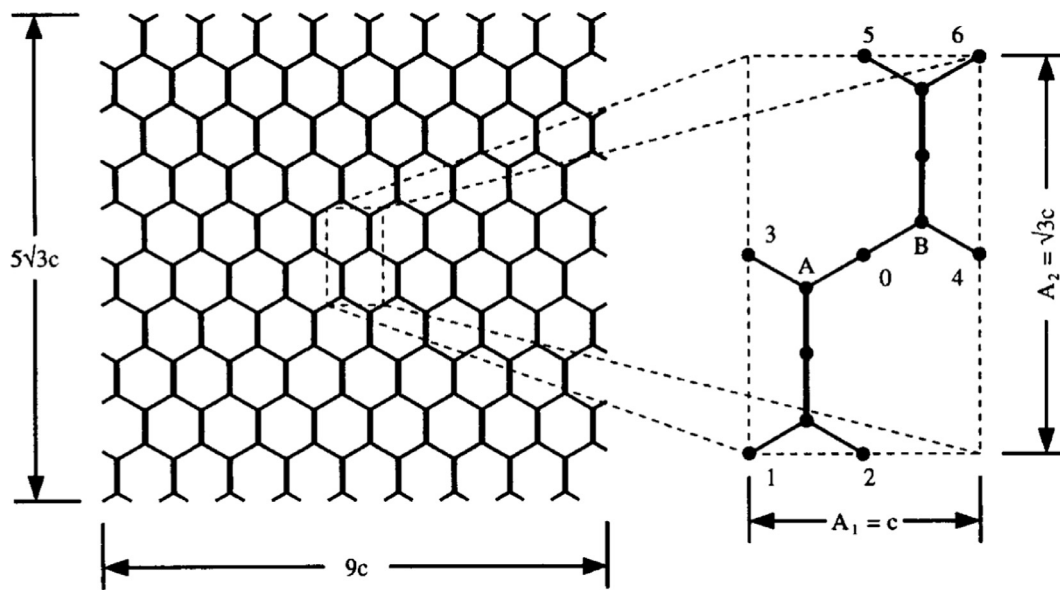
Fig. 6. Planar section of a perfect, infinite honeycomb, and chosen unit cell. From Triantafyllidis and Schraad (1998) with permission.

Fig. 7a shows the onset of failure surface for varying load paths, with $\theta = 0$ of particular interest in the current study. These results show that for most loading paths, the onset of plastic deformation, due to bending of the honeycomb cell sides, is the first failure mode to be encountered. However, there exists a regime of nearly equi-biaxial loading for which the onset of failure occurs due to bifurcation. Fig. 7b shows that within this loading regime the bifurcation mode is one that has a periodicity equal to that of the simulation unit cell. This is in contrast to the first bifurcation for loading paths with $|\Pi_1| \ll |\Pi_2|$, corresponding to $\phi \approx 3\pi/2$, for which the bifurcation mode is a long-wavelength, strain-like, deformation of the honeycomb. Of primary interest to the current study, the results of Triantafyllidis and Schraad (1998) show that under equi-biaxial loading honeycomb structures undergo initial failure due to elastic bifurcation and that this bifurcation is associated with a buckling mode that is periodic with a spatial wavelength that is of the same order of magnitude as the honeycomb cell size.

In a related study, Ohno et al. (2002) considered a three-dimensional rate based finite element formulation with an elastic constitutive relation to examine the behavior of hexagonal honeycomb structures with all cell sides of equal thickness. Using observed buckling patterns, a 2×2 four hexagon unit cell was selected for simulation within a homogenization framework and the onset of instability behavior was investigated for various proportional loading conditions. In this study the proportional loading paths correspond to specification of the principal *Cauchy stress* components. (This is in contrast to the previous investigation of Triantafyllidis and Schraad (1998), which takes the more physically realizable approach of controlling the components of the first Piola–Kirchhoff stress.) The authors found no loss of ellipticity (long wavelength instability, also called rank-one convexity), but instead found short wavelength bifurcation for all loading paths. Depending on the particular ratio of principal Cauchy stresses, one, two, or three critical deformation modes were identified at the onset of instability. The case of three critical modes corresponding to equi-biaxial compression. Based on the three critical deformation modes obtained numerically, Ohno et al. (2002) used ad-hoc arguments to conjecture that three equilibrium deformation patterns were possible for the post-bifurcation behavior of the honeycomb.

These modes are depicted in Fig. 8. The single critical mode, Mode I, was found to be the first instability associated with load-

ing paths where compressive loading is primarily aligned along the direction parallel to one hexagon cell side. When the loading is primarily aligned along the direction perpendicular to one hexagon cell side, then two simultaneous critical modes occur at the onset of instability and Mode II (a linear combination of two variants of Mode I) was predicted. Finally, when the loading is equi-biaxial, three critical modes occur at the onset of instability and Mode III was predicted.

2.3. Characterization of post-bifurcation behavior

Okumura et al. (2002) extended the work of Ohno et al. (2002) to numerically study the post-bifurcation dynamics of the elastic honeycomb structure under Cauchy stress control and displacement control loading conditions. The 2×2 four hexagon unit cell was used and artificial displacement constraints were applied, as needed, to ensure that only one instability mode occurred for each loading condition. Of particular interest for the current work, are the results for equi-biaxial loading. Okumura et al. (2002) found that for equi-biaxial displacement control Mode III was stable. Mode I and Mode II were unstable and found to dynamically transition to Mode III. In contrast, under Cauchy stress control Mode I and Mode II were found to be stable with Mode I having the lowest internal energy. Mode III was unstable and found to dynamically transition to Mode II. This result shows that the post-bifurcation behavior of the honeycomb is sensitive to the loading conditions. However, due to the somewhat unusual choice of controlling the Cauchy stress components, the physical interpretation of these dynamics simulations is somewhat problematic. Okumura et al. (2002) also report that the initial post-bifurcation behavior of Mode II and Mode III shows long wavelength instability (loss of rank-one convexity). Unfortunately, due to an apparent misunderstanding of the theory and its implications, Okumura et al. (2002) incorrectly dismiss this loss of ellipticity based on a faulty argument of incompatibility with their imposed boundary conditions.

The final work that we would like to highlight here is that of Saiki et al. (2005), who apply group theoretic methods to investigate the post-bifurcation behavior of the honeycomb structure. Based on the previous works, described above, Saiki et al. (2005) make the "sound engineering choice" to study the 2×2 four hexagon cell subjected to periodic boundary conditions. The authors first perform a purely theoretical bifurcation analysis based

a

b
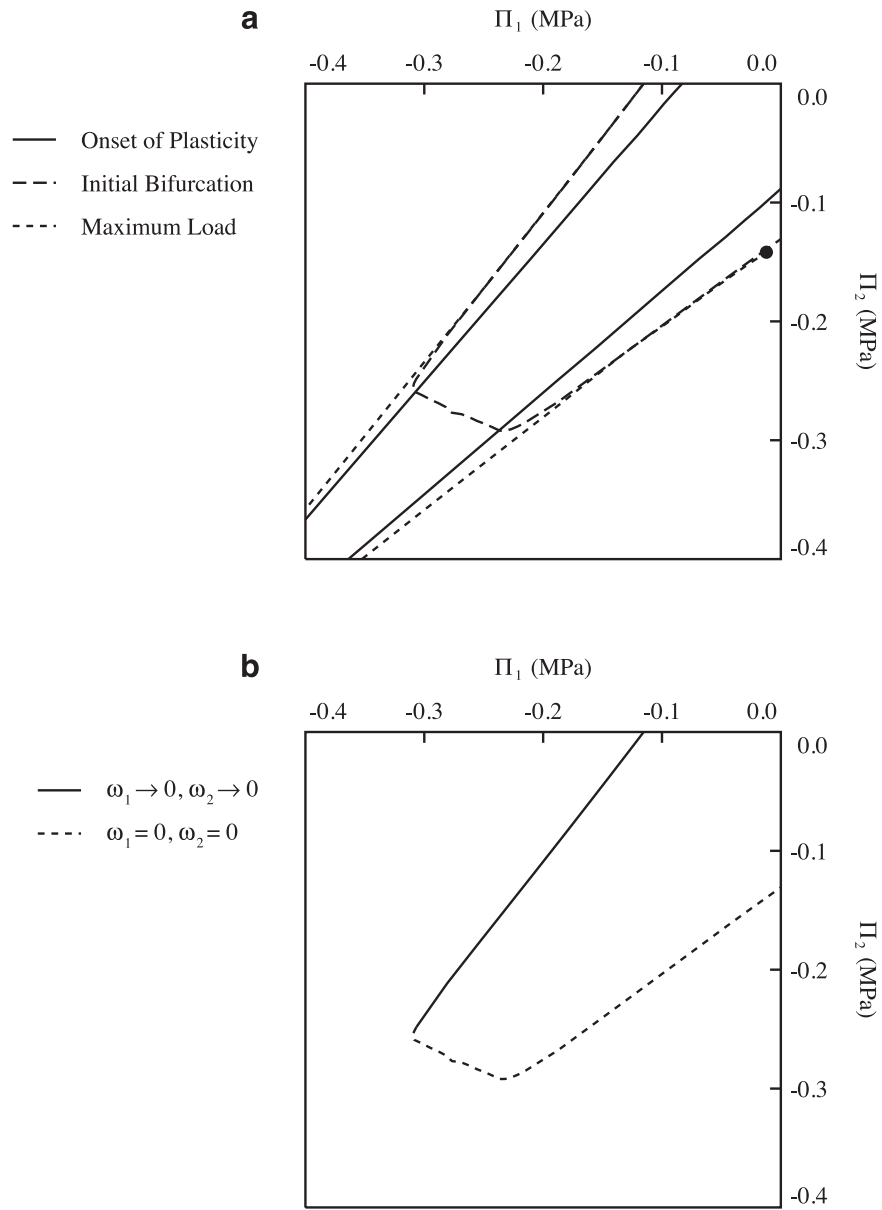
Fig. 7. (a) Onset of plasticity, initial bifurcation and maximum load surfaces in macroscopic stress space. (b) Regions of the initial bifurcation surface corresponding to two different bifurcation mode shapes. Here, Π_i are the principal components of the first Piola–Kirchhoff stress. From Triantafyllidis and Schraad (1998) with permission.
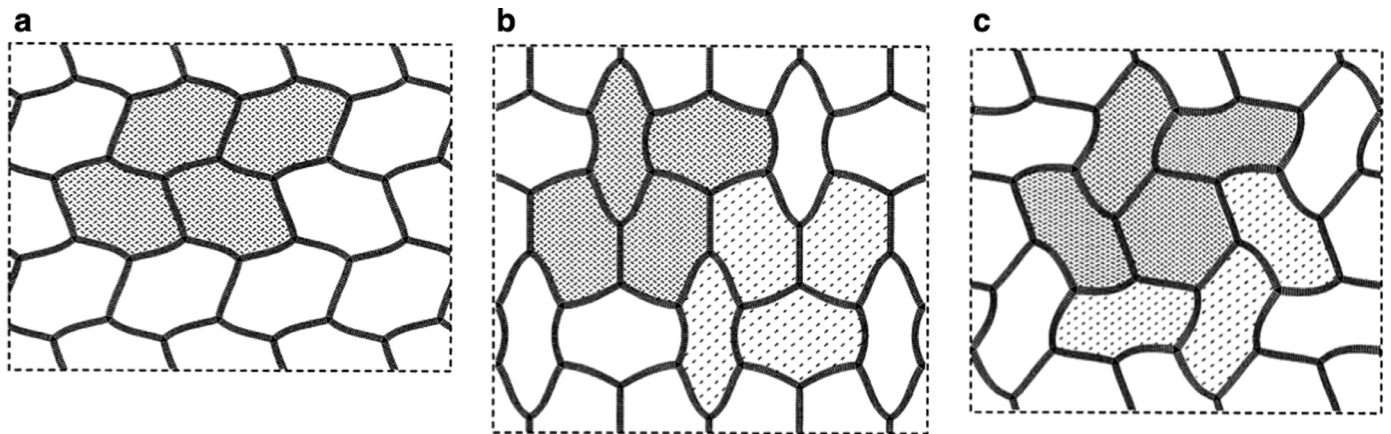
Fig. 8. Onset of instability buckling modes as suggested by Ohno et al. (2002). (a) Mode I (anti-rolls). (b) Mode II (rectangles). (c) Mode III (flower-mode). From Ohno et al. (2002) with permission.

on the nonlinear equilibrium equations for the 2×2 periodic honeycomb subjected to isotropic biaxial loading. This provides a set of equilibrium equations that is *equivariant* (symmetric) with respect to the symmetry group of the 2×2 unit cell, including D_6 (six-fold hexagonal rotations and mirror) symmetries, as well as *internal-translations*. From this analytical asymptotic bifurcation analysis, Saiki et al. (2005) review the well-known bifurcation results associated with breaking of D_6 symmetry and then derive new results for bifurcations associated with breaking of internal-translation symmetry. They show analytically that the post-bifurcating equilibrium paths that emerge from such a bifurcation point correspond precisely to the Mode I (anti-rolls), Mode II (rectangles), and Mode III (flower-mode) configurations that were previously proposed, using an ad-hoc technique, by Okumura et al. (2002).

In the second half of their work, Saiki et al. (2005) perform a numerical post-bifurcation analysis of the 2×2 four cell periodic honeycomb problem using a corotational large rotation and small strain Bernoulli–Euler beam formulation and a linearly elastic stress-strain model. The authors apply all-around displacement control boundary conditions to the periodic model corresponding to a macroscopically uniform dilatational contraction. Using this numerical model, the authors apply their group theory based bifurcation results in order to compute the initial post-bifurcation behavior associated with a series of internal-translation-breaking and D_6-symmetry-breaking bifurcations. These results provide a complete and rigorous investigation of the post-bifurcation behavior for the 2×2 four cell honeycomb subjected to equi-biaxial compression under displacement control. However, the authors do not address, in any manner, the stability of these post-bifurcated solutions.

From the literature review presented here, we have identified two significant open theoretical questions associated with the in-plane loading of honeycomb structures. First, the dependence of the structural response on the mechanical loading conditions has not been sufficiently explored and discussed, and second, the stability, with respect to perturbations of all wavelengths, of the post-bifurcated equilibrium solutions has not been investigated. In order to address these two issues, in the present work, we explore the stability of the honeycomb's post-bifurcated equilibrium solutions, using the Bloch wave method, and discuss how these solutions and their stability depend on three loading conditions: (i) displacement control, (ii) dead load Biot stress[3] control, and (iii) live load two-dimensional hydrostatic pressure control. Each of these loading conditions has a clear physical interpretation and provide interesting insight into the buckling behavior of the honeycomb.

3. Modeling

As with many of the researches discussed in the previous section, we model the hexagon cell honeycomb structure as a two-dimensional perfect periodic body of infinite extent. The solid sides (struts) of the hexagons are idealized as one-dimensional frame members capable of undergoing large displacements and rotations. The vertices where three hexagon sides come together are taken to behave as *welded* joints, which means that the three 120 degree angles between the three sides must remain the same during any deformation. However, the joint may undergo an overall rotation. The constitutive model for extension, bending, and shear of the frame members is taken to be linearly elastic. Based on the results of Triantafyllidis and Schraad (1998), the (initial) post-bifurcation equilibrium and stability behavior predicted by this model is applicable to all real hexagonal geometry honeycomb structures com-

Table 1
Geometry and elastic constant data used with the FEAP FEM program to model the honeycomb unit cell.

Hexagon side length (cm)	0.5
Strut thickness (cm)	0.05
Strut cross sectional area (cm^2)	0.05
Strut moment of inertia (cm^4)	1.041667×10^{-5}
Young's modulus (MPa)	69
Poisson's ratio	0.3

posed of rate-independent solids subjected to equi-biaxial compressive loadings.

3.1. Finite element discretization and numerical implementation

For any given calculation, an isolated unit cell of the honeycomb structure is selected and meshed with a finite element method (FEM) program. This provides the energy, forces, and stiffness as a function of the nodal degrees of freedom (DOFs) from the FEM code. Letting the FEM DOFs be given by $\mathbf{u} = (u_1, u_2, u_3, \ldots, u_N)$, these quantities may be represented as

$$w(\mathbf{u}), \tag{4}$$

$$\mathbf{f}(\mathbf{u}) \equiv -\frac{\partial w}{\partial \mathbf{u}}, \tag{5}$$

$$\mathbf{K}(\mathbf{u}) \equiv \frac{\partial^2 w}{\partial \mathbf{u} \, \partial \mathbf{u}}, \tag{6}$$

where N is equal to the number of DOFs per node times the number of nodes in the unit cell FEM mesh, w is the unit cell strain energy, $\mathbf{f}$ is the residual force, and $\mathbf{K}$ the tangent stiffness of the isolated unit cell for the arbitrary deformation $\mathbf{u}$ from the stress-free perfect hexagonal honeycomb reference configuration. Example unit cell FEM meshes as used in this work are shown in Fig. 9.

In this work the FEM code FEAP (Taylor, 2011) is used. The two-dimensional large displacement large rotation frame element with shear deformation included as part of the standard FEAP implementation is used with geometric parameters and elastic constants as given in Table 1. The geometric values are consistent with the small scale honeycomb specimens used by Papka and Kyriakides (1999a) and the material constants are consistent with typical values for the linearly elastic behavior of rubbers.

The nodal DOFs implemented by FEAP for this element are the nodal displacements in two directions and a nodal counterclockwise rotation in the plane. Thus, for node i the nodal DOF vector is $\mathbf{u}^{(i)} = (u_x^{(i)}, u_y^{(i)}, \theta^{(i)})$. The FEM mesh is constructed in such a way that nodes at the boundary of the isolated unit cell are matched into pairs corresponding to translation periodicity. Then the remaining *interior nodes* are numbered. This special numbering facilitates the application of periodic boundary conditions as described below.

In order to allow for the application of uniform deformation, periodic boundary conditions, and far-field loading, the FEM code is coupled with a custom code that applies displacement and rotation constraints in order to ensure that half the boundary nodes have displacements corresponding to an affine deformation and that the remaining (periodic) boundary nodes have displacements and rotations that satisfy appropriate periodicity conditions. In particular, the custom code imposes what we call *Lagrangian Cauchy–Born Kinematics* such that the deformed position $\mathbf{x}^{(i)}$ of each node is given by

$$\mathbf{x}^{(i)} = \mathbf{F}(\mathbf{X}^{(i)} + \mathbf{S}^{(i)}), \tag{7}$$

where $\mathbf{F}$ is the uniform deformation gradient tensor (with components F_{xx}, F_{xy}, F_{yx}, and F_{yy}), $\mathbf{X}^{(i)}$ is the reference position vector of

---

[3] The Biot stress loading is closely related to dead load first Piola–Kirchhoff stress loading. This is discussed more extensively in Elliott et al. (2011).
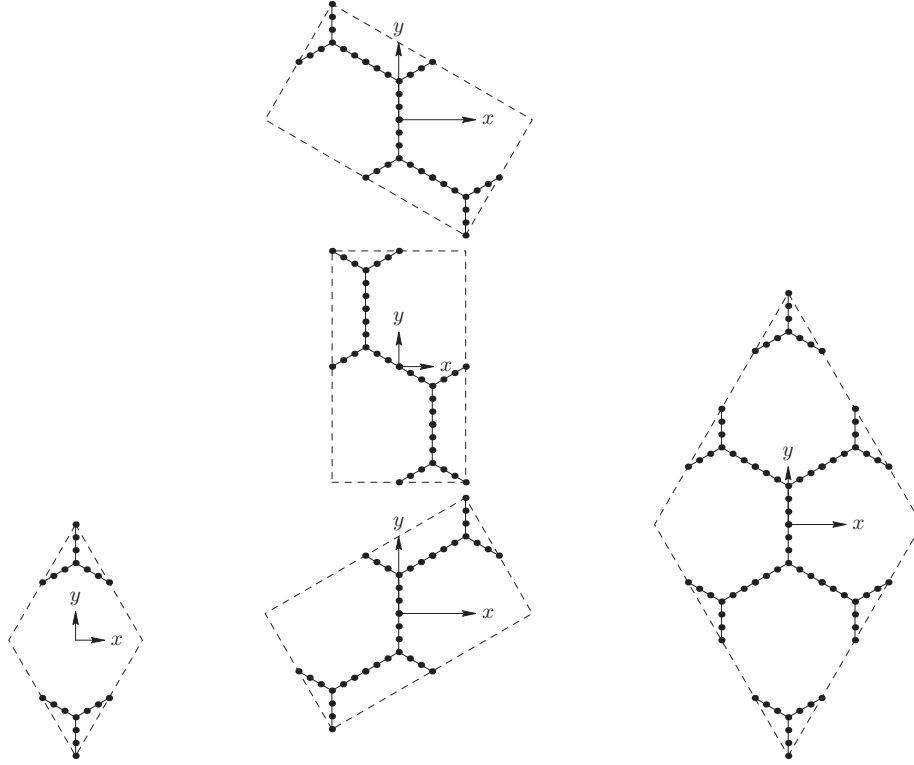
Fig. 9. 1×1, 1×2, and 2×2 unit cell FEM mesh examples.

node i, and $\mathbf{S}^{(i)}$ is the *reference shift vector* of node i. This kinematic choice, where the reference shift vector is acted upon by the uniform deformation mapping, allows for the natural description of macroscopically uniform deformation of the infinite structure. Thus, the custom code defines a DOF vector consisting of the components of the deformation gradient tensor, shift vectors and rotations for half the unit cell boundary nodes[4] and shift vectors and rotations for each interior node. In particular, the DOF vector is taken to be

$$\mathbf{v} = (\mathbf{F}, \bar{\mathbf{v}}) = (F_{xx}, F_{xy}, F_{yx}, F_{yy}, S_x^{(1)}, S_y^{(1)}, \theta^{(1)}, \dots, S_x^{(N_b/2)}, S_y^{(N_b/2)},$$
$$\theta^{(N_b/2)}, S_x^{(N_b+1)}, S_y^{(N_b+1)}, \theta^{(N_b+1)}, \dots, S_x^{(N_n)}, S_y^{(N_n)}, \theta^{(N_n)}), \quad (8)$$

where N_b is the number of boundary nodes in the unit cell mesh, and N_n is the total number of nodes in the isolated unit cell FEM mesh. The vector $\bar{\mathbf{v}}$ will be called the internal nodal degrees of freedom vector.

The kinematics of Eq. (7) implicitly define a mapping between the custom code DOF vector $\mathbf{v}$ and the FEM DOF vector $\mathbf{u}$, i.e., $\mathbf{u}(\mathbf{v})$. This mapping is used, along with the chain-rule for differentiation, to define the strain energy per reference primitive unit cell and its derivatives for the infinite honeycomb structure:

$$W(\mathbf{v}) \equiv \frac{1}{n} w(\mathbf{u}(\mathbf{v})), \quad (9)$$

$$\frac{\partial W}{\partial \mathbf{v}} \equiv \frac{1}{n} \frac{\partial w}{\partial \mathbf{u}} \frac{\partial \mathbf{u}}{\partial \mathbf{v}}, \quad (10)$$

$$\frac{\partial^2 W}{\partial \mathbf{v} \partial \mathbf{v}} \equiv \frac{1}{n} \left[\left(\frac{\partial^2 w}{\partial \mathbf{u} \partial \mathbf{u}} \frac{\partial \mathbf{u}}{\partial \mathbf{v}} \right) \frac{\partial \mathbf{u}}{\partial \mathbf{v}} + \frac{\partial w}{\partial \mathbf{u}} \frac{\partial^2 \mathbf{u}}{\partial \mathbf{v} \partial \mathbf{v}} \right], \quad (11)$$

---

[4] The periodic boundary conditions imply that only half of the boundary nodal DOFs are independent.

where n is the number of primitive unit cells contained within the chosen FEM unit cell.

Finally, in order to study the uniform equilibrium configurations of the honeycomb material when subjected to the three distinct far-field loading conditions considered in this work we define the following three total energy (per reference primitive unit cell) functions:

For dilatational displacement control: This loading condition corresponds to prescribing the deformation gradient tensor to have the form $\mathbf{F} = (1 - \Delta/2)\mathbf{I}$, where Δ is the non-dimensional scalar loading parameter (with $\Delta > 0$ corresponding to decreasing unit cell area) and $\mathbf{I}$ is the two-dimensional identity tensor. We define the total energy function for displacement control as

$$\bar{\mathcal{E}}(\bar{\mathbf{v}}; \Delta) \equiv W((1 - \Delta/2, 0, 0, 1 - \Delta/2, \bar{\mathbf{v}})). \quad (12)$$

For equi-biaxial Biot stress control: This loading condition adds the potential energy of a dead load Biot stress $\mathbf{P}_B = -\lambda \mathbf{I}$ conjugate to the strain measure $\mathbf{U} - \mathbf{I}$. Here, to avoid the complications associated with rigid-body rotations,[5] we restrict attention to pure stretches and introduce the reduced DOF vector

$$\mathbf{q} = (\mathbf{U}, \bar{\mathbf{v}}) = (U_{xx}, U_{yy}, U_{xy}, \bar{\mathbf{v}}). \quad (13)$$

Given a reduced DOF vector, $\mathbf{q} = (U_{xx}, U_{yy}, U_{xy}, \bar{\mathbf{v}})$ we can obtain the corresponding full DOF vector $\mathbf{v} = (U_{xx}, U_{xy}, U_{xy}, U_{yy}, \bar{\mathbf{v}})$ which may then be used as the argument to the honeycomb strain energy function $W(\mathbf{v})$. Thus, we obtain the total energy function for dead load control as

$$\hat{\mathcal{E}}(\mathbf{q}; \lambda) \equiv W((U_{xx}, U_{xy}, U_{xy}, U_{yy}, \bar{\mathbf{v}})) - \text{tr}(\mathbf{P}_B(\mathbf{U} - \mathbf{I})) A_{\text{cell}}$$
$$= W((U_{xx}, U_{xy}, U_{xy}, U_{yy}, \bar{\mathbf{v}})) + \lambda \text{tr}(\mathbf{U} - \mathbf{I}) A_{\text{cell}}, \quad (14)$$

---

[5] Note that rigid-body rotations are eliminated by the use of the symmetric right-stretch tensor in the definition of the reduced degree of freedom vector $\mathbf{q}$. Further, the use of the right-stretch tensor instead of the full deformation gradient eliminates the highly complicated bifurcation behavior associated with rigid-body rotations encountered at zero load. For an in-depth discussion of this bifurcation problem in a general setting, see Chillingworth et al. (1982, 1983).

where λ is the scalar loading parameter having physical dimensions of force per unit length ($\lambda > 0$ corresponds to compressive loading), and A_{cell} is the reference area of the primitive unit cell.

Finally for live two-dimensional hydrostatic pressure control: This loading condition adds the potential energy of a live hydrostatic load p, having physical dimensions of force per unit length, which is conjugate to the relative decrease in area of the primitive unit cell. Again, we restrict attention to pure stretches and obtain the total energy function for live load control as

$$\breve{\mathcal{E}}(\mathbf{q};\, p) \equiv W((U_{xx}, U_{xy}, U_{xy}, U_{yy}, \bar{\mathbf{v}})) + p[\det(\mathbf{U}) - 1]A_{\text{cell}}, \qquad (15)$$

where $\det(\mathbf{U}) = a_{\text{cell}}/A_{\text{cell}}$ gives the ratio of deformed to reference unit cell area.

4. Equilibrium and stability

In this section we state the equilibrium equations for each loading condition, discuss the elimination of rigid-body translations from the equilibrium equation solution sets, and discuss the evaluation of stability for the obtained equilibrium solutions. Then we identify the numerical path-following strategy that is used to map out the equilibrium solutions as a function of the loading parameter for each loading condition, and comment on the handling of bifurcation points where two or more equilibrium paths intersect.

4.1. Equilibrium configurations

We apply the principle of stationary potential energy and obtain equilibrium equations, which implicitly define the equilibrium configurations, by setting the first derivative of the total energy equal to zero

$$\frac{\partial \bar{\mathcal{E}}(\bar{\mathbf{v}};\, \Delta)}{\partial \bar{\mathbf{v}}} = \mathbf{0}, \qquad \frac{\partial \hat{\mathcal{E}}(\mathbf{q};\, \lambda)}{\partial \mathbf{q}} = \mathbf{0}, \qquad \frac{\partial \breve{\mathcal{E}}(\mathbf{q};\, p)}{\partial \mathbf{q}} = \mathbf{0}. \qquad (16)$$

With $\bar{\mathbf{v}} \in \mathbb{R}^M$ (as defined in (8)) and $\mathbf{q} \in \mathbb{R}^{M+3}$ (as defined in (13)), these correspond to systems of nonlinear algebraic equations of size M, $M + 3$, and $M + 3$, respectively. Each system of equations also has a single loading parameter (Δ, λ, and p, respectively).

4.1.1. Elimination of rigid-body translations

As defined in Section 3, the total energy functions are invariant to rigid-body translations in the two spatial directions, corresponding to DOF vectors where all internal shift vectors are equal. Configurations that differ only by a rigid-body translation are considered physically equivalent. This implies that the space of all configurations can be partitioned into equivalence classes consisting of configurations that differ only by a rigid-body translation. An additional consequence of the energy invariance with respect to rigid-body displacements is that the equilibrium Eqs. (16) are insensitive to such changes in configuration. In particular, it is easy to show that, for all $\mathbf{t} = (0, 0, 0, \tilde{\mathbf{t}}) \in \mathbb{T} \subset \mathbb{R}^M$ where $\mathbb{T}$ is the translation subspace of configurations,

$$\frac{\partial \bar{\mathcal{E}}(\bar{\mathbf{v}};\, \Delta)}{\partial \bar{\mathbf{v}}} \cdot \tilde{\mathbf{t}} = 0, \qquad \frac{\partial \hat{\mathcal{E}}(\mathbf{q};\, \lambda)}{\partial \mathbf{q}} \cdot \mathbf{t} = 0, \qquad \frac{\partial \breve{\mathcal{E}}(\mathbf{q};\, p)}{\partial \mathbf{q}} \cdot \mathbf{t} = 0, \qquad (17)$$

for all $(\bar{\mathbf{v}};\, \Delta)$, $(\mathbf{q};\, \lambda)$ and $(\mathbf{q};\, p)$, respectively. Thus, if a configuration $\mathbf{q}_0$ satisfies Eq. (16), then so does $\mathbf{q}_0 + \mathbf{t}$ for every $\mathbf{t} \in \mathbb{T}$.

It is desirable to modify the energy functions in such a way that only one representative from each equivalence class is identified as an equilibrium configuration.[6] We achieve this goal by adding a so-

called *Phantom energy* (Jusuf, 2010) term to obtain

$$\bar{\mathcal{E}}^\star(\bar{\mathbf{v}};\, \Delta) \equiv \bar{\mathcal{E}}(\bar{\mathbf{v}};\, \Delta) + \frac{1}{2}\left[\sum_{i=1}^{N_b/2} S_x^{(i)} + \sum_{i=N_b+1}^{N_n} S_x^{(i)}\right]^2$$
$$+ \frac{1}{2}\left[\sum_{i=1}^{N_b/2} S_y^{(i)} + \sum_{i=N_b+1}^{N_n} S_y^{(i)}\right]^2, \qquad (18)$$

$$\hat{\mathcal{E}}^\star(\mathbf{q};\, \lambda) \equiv \hat{\mathcal{E}}(\mathbf{q};\, \lambda) + \frac{1}{2}\left[\sum_{i=1}^{N_b/2} S_x^{(i)} + \sum_{i=N_b+1}^{N_n} S_x^{(i)}\right]^2$$
$$+ \frac{1}{2}\left[\sum_{i=1}^{N_b/2} S_y^{(i)} + \sum_{i=N_b+1}^{N_n} S_y^{(i)}\right]^2, \qquad (19)$$

$$\breve{\mathcal{E}}^\star(\mathbf{q};\, p) \equiv \breve{\mathcal{E}}(\mathbf{q};\, p) + \frac{1}{2}\left[\sum_{i=1}^{N_b/2} S_x^{(i)} + \sum_{i=N_b+1}^{N_n} S_x^{(i)}\right]^2$$
$$+ \frac{1}{2}\left[\sum_{i=1}^{N_b/2} S_y^{(i)} + \sum_{i=N_b+1}^{N_n} S_y^{(i)}\right]^2, \qquad (20)$$

where the additional terms are positive semi-definite and have value zero only for configurations with zero rigid-body displacement. This ensures that only zero rigid-body displacement configurations are solutions to the corresponding equilibrium equations,

$$\frac{\partial \bar{\mathcal{E}}^\star}{\partial \bar{\mathbf{v}}} = \mathbf{0}, \qquad \frac{\partial \hat{\mathcal{E}}^\star}{\partial \mathbf{q}} = \mathbf{0}, \qquad \frac{\partial \breve{\mathcal{E}}^\star}{\partial \mathbf{q}} = \mathbf{0}. \qquad (21)$$

4.1.2. Stability of an equilibrium configuration

The identified equilibrium configurations are infinite periodic structures with various *far-field* loading conditions applied. Practical stability definitions for such infinite problems are hard to formulate and justify. A more reasonable approach is to formulate the definitions and ideas of stability in terms of boundary value problems (BVPs) for finite bodies. This may be achieved in a reasonably straight-forward fashion; for example, see Truesdell and Toupin (1960) and Como and Grimaldi (1995). In such a framework, there is a natural definition for the stability of an equilibrium configuration for a BVP. Engineers like to think of a loss of stability as being either a *structural instability* or a *material instability*. Structural instability, such as column buckling, is typically driven by geometric nonlinearities. Material instability, such as shear-banding or phase transformation, is typically thought of as *anything that is not a structural instability*. Unfortunately, these engineering concepts cannot be precisely defined. In practice, one identifies various *material stability criteria* which are point-wise conditions (specified in terms of the properties of a material's constitutive relation) that are *necessary* for stability of an equilibrium configuration for all possible BVPs. In particular, here we will think of the strain energy function $W(\mathbf{v})$ presented in Section 3 as a material constitutive law and consider the classic stability condition of local[7] *rank-one convexity* (Como and Grimaldi, 1995; Truesdell et al., 2004). This condition concerns the elastic moduli (second derivatives) of the *homogenized continuum* (see Elliott et al., 2006b) energy density $\widetilde{W}(\mathbf{F})$. These moduli are obtained by statically condensing the

---

[6] See Footnote 5.

[7] Here *local* refers to the fact that we only consider the criterion evaluated for deformation gradient $\mathbf{F}_0$ associated with the uniform equilibrium configuration of interest.

internal nodal degrees of freedom from $W(\mathbf{v})$ and are given by[8]:

$$\frac{\partial^2 \widetilde{W}}{\partial \mathbf{F} \partial \mathbf{F}} = \frac{\partial^2 W}{\partial \mathbf{F} \partial \mathbf{F}} - \frac{\partial^2 W}{\partial \mathbf{F} \partial \bar{\mathbf{v}}} \left(\frac{\partial^2 W}{\partial \bar{\mathbf{v}} \partial \bar{\mathbf{v}}} \right)^{-1} \frac{\partial^2 W}{\partial \bar{\mathbf{v}} \partial \mathbf{F}}. \tag{22}$$

In terms of these homogenized continuum moduli, the local rank-one convexity (RK1) stability condition says that in order for the uniform equilibrium configuration characterized by $\mathbf{v}_0 = (\mathbf{F}_0, \bar{\mathbf{v}}_0)$ to be stable, it is necessary that

$$(\mathbf{a} \otimes \mathbf{k}) : \left. \frac{\partial^2 \widetilde{W}}{\partial \mathbf{F} \partial \mathbf{F}} \right|_{\mathbf{F}=\mathbf{F}_0} : (\mathbf{a} \otimes \mathbf{k}) > 0, \tag{23}$$

for all non-zero vectors $\mathbf{a}$ and $\mathbf{k}$. This condition is also known as the *strong ellipticity* criterion (Truesdell et al., 2004).

For a periodic microstructured material model such as the one studied here, the RK1 condition should be generalized by considering periodic perturbations on all possible unit cells. This corresponds to the *Phonon or Bloch wave stability* criterion as discussed in depth by Elliott et al. (2006b). The Bloch wave criterion considers all bounded perturbations of the equilibrium configuration, and is a set of necessary conditions for the configuration to be an energy minimizing state. The criterion is equivalent to requiring all positive eigenvalues, associated with eigenvectors of the form $\delta \mathbf{v} = (\mathbf{0}, \delta \bar{\mathbf{v}})$, for the Hessian of the unit cell energy for all possible unit cells. The Bloch theorem (Geymonat et al., 1993) ensures that these eigenvectors of the Hessian of the unit cell energy may be written as follows. Starting with a primitive unit cell for the equilibrium configuration, which has lattice vectors $\mathbf{G}_1$ and $\mathbf{G}_2$ and FEM nodes numbered $j = 1, 2, \ldots, m$, we can label each node in the extended non-primitive unit cell in terms of its primitive unit cell image indices (ℓ^1, ℓ^2, j), with ℓ^1 and ℓ^2 integers. Thus, the reference position of node (ℓ^1, ℓ^2, j) is given in terms of the reference position of node $(0, 0, j)$ as

$$\mathbf{X}(\ell^1, \ell^2, j) \equiv \ell^1 \mathbf{G}_1 + \ell^2 \mathbf{G}_2 + \mathbf{X}(0, 0, j).$$

Now, the Bloch theorem says that eigen-perturbations (also called *Bloch waves*) for the equilibrium configuration can be written as

$$\delta \mathbf{u}(\ell^1, \ell^2, j) = \delta \mathbf{u}(0, 0, j) \sum_{\mathbf{k}} \exp \left(\mathbf{k} \cdot \mathbf{X}(\ell^1, \ell^2, j) \right), \tag{24}$$

where $\mathbf{k} = 2\pi i (k_1 \mathbf{G}^1 + k_2 \mathbf{G}^2)$ is the eigen-perturbation *wave vector* written with respect to the primitive unit cell reciprocal lattice vectors $\mathbf{G}^1$ and $\mathbf{G}^2$ and scaled by a factor of $2\pi i$, with i the unit imaginary number. Due to the periodicity of the Bloch wave expression, only $\mathbf{k}$ vectors from the *First Brillouin Zone* (BZ) need to be considered, as described by Dove (1993). Fig. 10 shows the lattice vectors and reciprocal lattice vectors, along with the fully symmetric first BZ, for the undeformed hexagonal honeycomb structure.

The primitive unit cell perturbation $\delta \mathbf{u}(0, 0, j)$ in Eq. (24) is not determined by the Bloch theorem, but in general depends on the wave vector $\mathbf{k}$. In particular, it is determined by solving an eigenvalue problem on the primitive unit cell (which has $3m$ degrees of freedom corresponding to two spatial displacement components and one rotation for each FEM node). Thus, for each wave vector $\mathbf{k}$ there will be $3m$ distinct eigenvectors $\delta \mathbf{u}(0, 0, j; \mathbf{k}, h)$, where $h \in \{1, 2, \ldots, 3m\}$ is a label distinguishing each eigenvector. Associated with each eigenvector is an eigenvalue $\Lambda(\mathbf{k}, h)$. Thus, the Bloch wave stability condition says that in order for the uniform
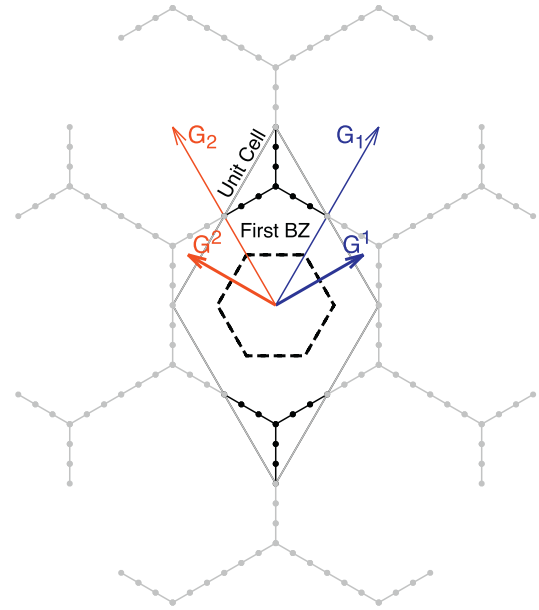

Fig. 10. Lattice vectors, reciprocal lattice vectors, and fully symmetric First Brillouin Zone for the hexagonal honeycomb lattice.

equilibrium configuration to be stable, it is necessary that[9]

$$\min_{\mathbf{k}, h} \Lambda(\mathbf{k}, h) > 0. \tag{25}$$

The different Bloch wave eigenvalues for each wave vector $\mathbf{k}$ can, for wave vectors in a neighborhood of the so-called Γ-point $\mathbf{k} = \mathbf{0}$, be usefully split into two categories: *acoustic* eigenvalues that are associated with Bloch wave deformation patterns that have a slow spatial variation (i.e., *long wavelength* modes), and *optic* eigenvalues that are associated with Bloch wave deformation patterns that have a rapid spatial variation (i.e., *short wavelength* modes).

In principle, Eq. (25) involves an infinite set of wave vectors taken from the first BZ over which the Bloch wave criterion must be evaluated. This is, of course, not possible and therefore a finite grid of wave vectors is selected for evaluation of the Bloch wave criterion. However, due to the existence of the unit cell energy, and thus the symmetry of its Hessian, the Bloch wave eigenvalues satisfy the identity $\Lambda(-\mathbf{k}, h) = \Lambda(\mathbf{k}, h)$. Further, considering the rotational symmetry of the problem one finds that only $\mathbf{k}$ vectors from the irreducible part of the Brillouin zone provide independent Bloch wave eigenvalues that must be considered in order to evaluate the Bloch wave stability condition. Fig. 11 shows a plot of Bloch wave eigenvalue contours for the hexagonal honeycomb structure.

Although the irreducible BZ provides the smallest domain of independent Bloch wave eigenvalues, this domain changes size once the structure is deformed and the hexagonal symmetry is broken. To avoid such complexities in our Bloch wave algorithms, we prefer to use a $\mathbf{k}$ vector grid over a full one-half of the first BZ. That is, we consider wave vector components that satisfy $-1/2 < k_1 \leq 1/2$, and $0 \leq k_2 \leq 1/2$, as indicated by the *computed zone* labeled in Fig. 11. Using this region takes advantage only of the lattice inversion property of the material's translational symmetry group and, thus, guarantees that our algorithm will work correctly for all deformed configurations of the honeycomb. Additional details related

---

[8] Note, some care must be taken to eliminate the zero-eigenvalues of $\frac{\partial^2 W}{\partial \bar{\mathbf{v}} \partial \bar{\mathbf{v}}}$ associated with rigid-body translations when computing the inversion indicated in Eq. (22).

[9] It must be noted that when $\mathbf{k} = \mathbf{0}$ there will be two zero eigenvalues corresponding to rigid-body translation. We do not wish to consider such rigid-body motions as instabilities, and therefore, (implicitly) exclude these eigenvalues from consideration in Eq. (25).
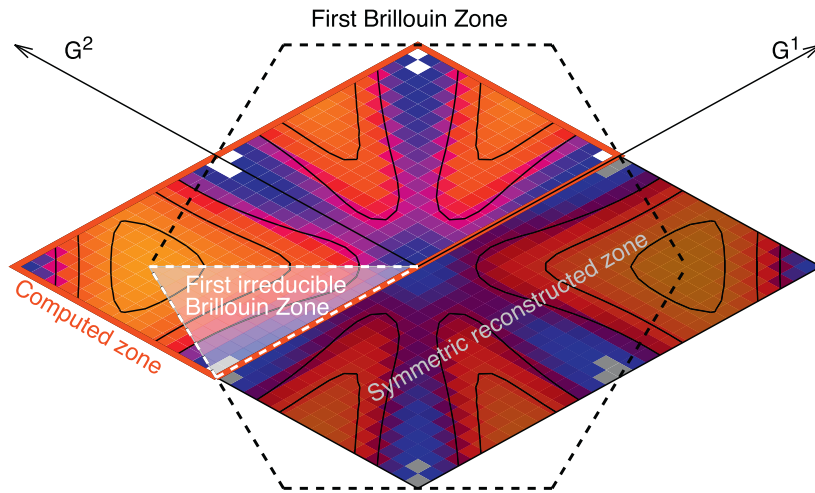
Fig. 11. Contour plot showing the Bloch wave eigenvalues as a function over **k** vector space. The contours are plotted over a two-by-two set of primitive reciprocal unit cells so that the full rotational symmetry of the contours may be observed. The fully symmetric first BZ is shown by the dotted lines. It is clear to see that the eigenvalue contours exhibit the hexagonal symmetry of the perfect honeycomb lattice. The irreducible BZ is also shown.
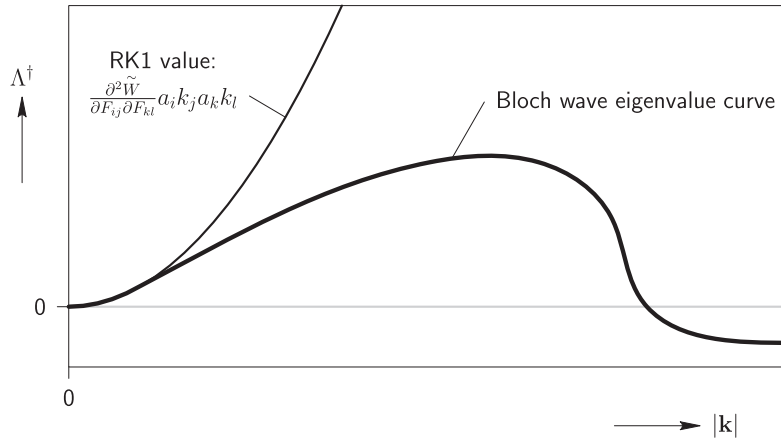

Fig. 12. Schematic showing the relationship between the RK1 criterion and the Bloch wave criterion. Positive values of the RK1 criterion correspond to positive initial curvature of the corresponding acoustic Bloch wave eigenvalue curve. In the hypothetical situation depicted the equilibrium configuration satisfies the RK1 criterion (positive initial curvature) but violates the Bloch wave criterion due to the negative Bloch wave eigenvalues for larger |**k**|.

to the Bloch wave stability condition as used and implemented in this work can be found in Elliott et al. (2006b).

It is useful to emphasize that the RK1 and Bloch wave criteria are independent of the effects of the applied loading, in the sense that they depend only on the strain energy function $W(\mathbf{v})$ and not the total energies of Eqs. (12), (14), and (15). For any BVP that has the uniformly deformed state of interest as an equilibrium configuration, both the RK1 and Bloch wave criteria are *necessary conditions* for the equilibrium configuration to be stable. In particular, this is true even for the BVP of place (i.e., all-around displacement conditions), in which case these conditions are also sufficient (Geymonat et al., 1993; Truesdell et al., 2004).

The RK1 criterion is satisfied if the Bloch wave criterion is satisfied.[10] However, the converse is not true. Indeed, it can be shown (Elliott et al., 2006b) that the RK1 expression provides the initial curvature of the corresponding Bloch wave acoustic eigenvalue curve for **k** near the Γ-point. If this initial curvature is positive the RK1 criterion is satisfied and all acoustic Bloch wave eigenvalues near the Γ-point are positive. However, if the initial curvature

is negative, then the RK1 criterion is violated and there exist at least some negative Bloch wave eigenvalues. Of course, it is possible that all of the initial curvatures are positive and there exist negative Bloch wave eigenvalues (these could be associated with optic eigenvalues or eigenvalues for **k** not near the Γ-point). Fig. 12 illustrates the relationship between the RK1 criterion and the Bloch wave criterion for a hypothetical situation where the RK1 criterion is satisfied but the Bloch wave criterion is violated.

For some particular all-around traction or mixed BVPs, it is possible to establish additional local conditions on the total energy (Eqs. (14) and (15)) that are also necessary for stability of that BVP's equilibrium configuration. Various authors have attempted to define such criteria (for example, see the *Cauchy–Born stability criterion* of Elliott et al. (2006b)), but often such criteria are only applicable to a very special set of BVPs and in many cases the precise conditions for which such stability criteria are applicable are not clearly specified. A particularly common situation is for authors to simply claim that positive-definiteness of whatever energy function they happen to be working with is a stability criterion. For example,

---

[10] Although the RK1 criterion is implied by the Bloch wave criterion (and is, in principle, redundant), it is convenient computationally to use both criteria. That is, use of the RK1 criterion eliminates the need to be concerned with using a small enough **k** vector grid spacing in order to capture the correct behavior near the Γ-point.

$$\delta\bar{\mathbf{v}} \cdot \left(\left.\frac{\partial^2 \bar{\mathcal{E}}^\star}{\partial\bar{\mathbf{v}}\partial\bar{\mathbf{v}}}\right|_{\bar{\mathbf{v}}=\bar{\mathbf{v}}_0} \delta\bar{\mathbf{v}} \right) > 0 \quad \forall \quad \delta\bar{\mathbf{v}} \neq \mathbf{0}, \tag{26}$$

for the dilatational displacement control energy of Eq. (12), or

$$\delta\mathbf{q} \cdot \left(\left. \frac{\partial^2 \hat{\mathcal{E}}^\star}{\partial\mathbf{q}\partial\mathbf{q}} \right|_{\mathbf{q}=\mathbf{q}_0} \delta\mathbf{q} \right) > 0 \qquad \forall \quad \delta\mathbf{q} \neq \mathbf{0}, \tag{27}$$

for the equi-biaxial Biot dead loading energy of Eq. (14), or

$$\delta\mathbf{q} \cdot \left(\left. \frac{\partial^2 \breve{\mathcal{E}}^\star}{\partial\mathbf{q}\partial\mathbf{q}} \right|_{\mathbf{q}=\mathbf{q}_0} \delta\mathbf{q} \right) > 0 \qquad \forall \quad \delta\mathbf{q} \neq \mathbf{0}, \tag{28}$$

for the live hydrostatic loading energy of Eq. (15). In this paper we will indicate the predictions of these *ad-hoc stability criteria* alongside those of the rigorous RK1 and Bloch wave criteria in order to illustrate how they can lead to incorrect conclusions.

4.2. Equilibrium branches and their bifurcations

The solution sets to the modified equilibrium Eqs. (21) are generally path-connected. In other words, Eqs. (21) serve to implicitly define a *path* or *branch* of configurations ($\bar{\mathbf{v}}(\Delta)$, $\mathbf{q}(\lambda)$, and $\mathbf{q}(p)$, respectively) corresponding to a sequence of equilibrium solutions for different values of the loading parameter.

4.2.1. Paths of equilibrium configurations

In order to numerically solve Eqs. (21) and follow an equilibrium branch for a particular loading condition, arc-length continuation (branch-following) methods are used (Allgower and Georg, 2003; Elliott et al., 2011; Jusuf, 2010; Pattamatta et al., 2014). These techniques allow the numerical solution procedure to follow the equilibrium branch across critical points corresponding to limit-loads (where the equilibrium branch reaches a turning point—local maximum or minimum—with respect to the loading parameter). Further, the use of adaptive arc-length step size techniques provide a high-fidelity representation of the equilibrium branch that can be obtained with a minimum of computational effort.

In the study of structures, such as honeycomb materials, with high amounts of symmetry (including rotational, mirror, and translational) it is important to take advantage of these symmetries in order to simplify the solution and analysis of the equilibrium equations. Accordingly, we have used techniques from group theory (Elliott et al., 2006a; Healey, 1988; Ikeda and Murota, 2010; Jusuf, 2010; Pattamatta et al., 2014) to further modify the equilibrium equations in order to isolate the particular equilibrium branch of interest and to reduce the computational effort necessary for the numerical solution of the equilibrium equations.

4.2.2. Bifurcation of equilibrium paths

Bifurcation points are equilibrium configurations where two or more distinct equilibrium paths intersect. These points can be identified by the existence of a zero eigenvalue of the unit cell energy's Hessian or by a zero Bloch wave eigenvalue[11] $\Lambda(\mathbf{k}, h)$. Such zero eigenvalues are typically associated with the transition of a deformation mechanism from stable-to-unstable (where the eigenvalue goes from positive to negative) or from unstable-to-stable (where the eigenvalue goes from negative to positive) along an equilibrium path. Therefore, bifurcation points along a path can be identified by monitoring the eigenvalues of the energy's Hessian and the Bloch wave eigenvalues for a change in their algebraic sign. Once the existence of a bifurcation point between two numerical solution points along an equilibrium path has been identified in

this manner, a bi-section-like algorithm is used to obtain a highly accurate numerical representation of the bifurcation point (Jusuf, 2010).

If the bifurcation point is associated with a Hessian eigenvalue being zero, then all equilibrium paths that cross at the bifurcation point have (at least) the same translational periodicity of the unit cell used to compute the equilibrium path along which the bifurcation point was discovered. In this case, a bifurcation analysis is conducted, using symmetry methods (Healey, 1988; Ikeda and Murota, 2010; Wohlever and Healey, 1995) and asymptotic expansions (Elliott et al., 2006a; Ikeda and Murota, 2010; Triantafyllidis and Peek, 1992) based on the Lyapunov–Schmidt–Koiter decomposition. The asymptotic analysis leads to the *bifurcation equations* (Triantafyllidis and Peek, 1992)

$$\sum_{j,k=1}^{H} \alpha_j \alpha_k \mathcal{E}_{ijk} + 2\lambda_1 \sum_{j=1}^{H} \alpha_j \mathcal{E}_{ij\lambda} = 0; \qquad i = 1, \ldots, H; \tag{29}$$

for asymmetric bifurcation and

$$\sum_{j,k,l=1}^{H} \alpha_j \alpha_k \alpha_l \mathcal{E}_{ijkl} + 3\lambda_2 \sum_{j=1}^{H} \alpha_j \mathcal{E}_{ij\lambda} = 0; \qquad i = 1, \ldots, H; \tag{30}$$

for symmetric bifurcation. Here, H is the multiplicity of the bifurcation point (number of zero Hessian eigenvalues), α_i and λ_1 are the components of the initial tangent for a bifurcating path, λ_2 is the initial curvature of a symmetric bifurcation path, $\mathcal{E}_{ijk}$ and $\mathcal{E}_{ij\lambda}$ are related to third-order derivatives of the energy evaluated at the bifurcation point, and $\mathcal{E}_{ijkl}$ is related to forth-order derivatives of the energy evaluated at the bifurcation point. Group theory methods (to be described more completely in a forthcoming article) are used to help solve these equations for the α_i and λ_1 or λ_2. Each solution is associated with a bifurcating equilibrium path. These solutions are then used to construct a prediction for an equilibrium point along each bifurcating path. From this information the branch-following methods, described in the previous section, may be initialized in order to follow all of the bifurcating equilibrium paths that intersect at the identified bifurcation point. This approach to branch-switching is quite robust as it avoids the need to introduce an ad-hoc imperfection mode and amplitude for use with the heuristic imperfection method.

If the bifurcation point is associated with a Bloch wave eigenvalue being zero, then the bifurcating equilibrium paths that cross the bifurcation point have less translational symmetry (a strict sub-group relationship) than the unit cell used to compute the equilibrium path along which the bifurcation point was discovered. In this case, the Cascading-Cauchy–Born algorithm described by Sorkin et al. (2014) is first used to identify a new, larger, unit cell with which the bifurcating equilibrium paths may be computed. Once the appropriate unit cell is identified, a bifurcation analysis like the one described for Hessian bifurcations is performed and the resulting post-bifurcation expressions for the bifurcating paths may be used to initialize the branch-following methods and to numerically compute the new equilibrium paths.

In this manner, the solution set to the equilibrium Eqs. (21) is mapped out and, by evaluating the RK1 and Bloch wave conditions, statements about the stability of each equilibrium configuration may be made.

5. Results

In this section we explore the equi-biaxial compression behavior of a hexagonal cell honeycomb under three distinct far-field loading conditions. We start with a primitive unit cell of the honeycomb and compute the principal equilibrium path and its

---

[11] Since every Bloch wave with rational components k_1 and k_2 can be represented using an appropriately-sized periodic unit cell, it is understood that a zero Bloch wave eigenvalue guarantees the existence of a zero eigenvalue of the corresponding unit cell energy's Hessian. Thus, zero Bloch wave eigenvalues are seen to be associated with bifurcation for the equilibrium equations obtained from the appropriately-sized periodic unit cell energy function.
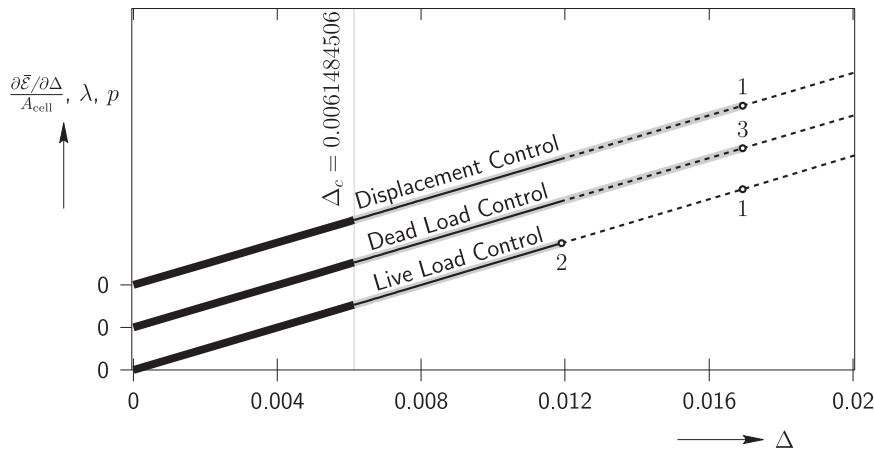
Fig. 13. Primitive unit cell principal equilibrium path and its stability for each type of far-field loading. The horizontal axis corresponds to the compressive Biot strain ($\Delta = \text{tr}(\mathbf{I} - \mathbf{U})$), whereas the vertical axis displays an appropriate stress-like quantity. Heavy solid line segments indicate stability with respect to both RK1 and Bloch wave stability criteria (as well as the ad-hoc criterion). Thin solid line segments with a light background indicate equilibrium configurations that are RK1 (and ad-hoc) stable but Bloch wave unstable. Dashed line segments with a light background indicate equilibrium configurations that are stable only with respect to the ad-hoc criterion. Finally, plain dashed line segments are unstable with respect to all stability criteria considered in this work. Open circles with numbers on the paths correspond to Hessian bifurcation points and indicate the number of eigenvalues that become zero simultaneously.
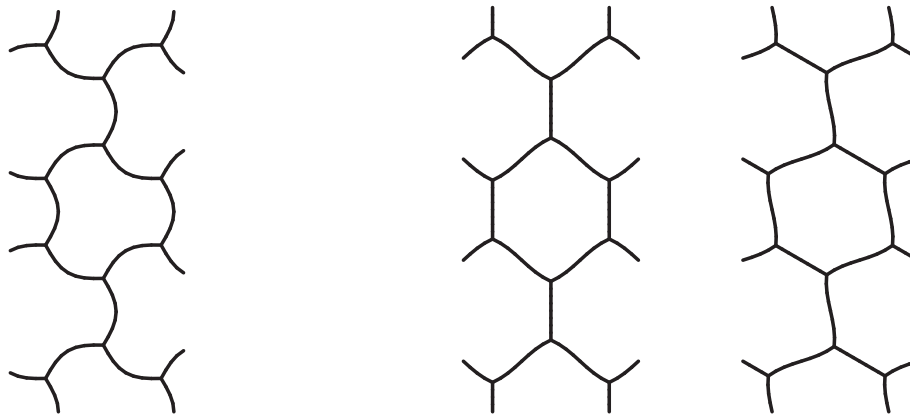

Fig. 14. Primitive unit cell Hessian bifurcation modes. Left: simple three-fold symmetric bifurcation mode. Right: two two-fold symmetric deformations making up a (symmetry adapted) basis for the double bifurcation point. Multiple copies of the deformed primitive unit cell are shown so as to make the resulting deformation pattern more easily recognizable.

stability. Then we explore the unit cell bifurcations and Bloch wave bifurcations that occur along the principal path. The corresponding bifurcated equilibrium paths are computed and their stability is evaluated and discussed.

5.1. Primitive unit cell behavior

5.1.1. Principal equilibrium path and its stability

A primitive unit cell (1 × 1), as shown on the left in Fig. 9, was used to compute solutions to the modified equilibrium Eqs. (21) as described in Section 4. The resulting load–deformation curves are shown in Fig. 13.

The figure shows the compressive Biot strain ($\Delta = \text{tr}(\mathbf{I} - \mathbf{U})$) on the horizontal axis with a stress-like quantity along the vertical axis. For displacement control, $\frac{\partial \bar{\mathcal{E}}/\partial \Delta}{A_{\text{cell}}}$ is plotted. For dead load and live load control, the loading parameter λ and p, respectively, is plotted. The curves are translated vertically with respect to each other in order to make each curve clearly visible. Thus, the vertical axis origin is different for each curve as indicated in the figure. However, the vertical axis scale is the same for each curve. The first thing we notice about these curves is that they are (very nearly) straight lines. This is expected due to the linearly elastic material constitutive law adopted in this work, the

hexagonal symmetry of the honeycomb, and the isotropic nature of each loading device. These factors lead to a principal equilibrium path that corresponds to pure dilatational deformation of the honeycomb structure. The stress-like parameters along the principal paths for the three loading devices are related according to $\frac{\partial \bar{\mathcal{E}}/\partial \Delta}{A_{\text{cell}}} = \lambda = (2 - \Delta)p$.

Next, we turn our attention to the stability of the honeycomb's principal paths. In Fig. 13 heavy solid line segments indicate stability with respect to both the RK1 and Bloch wave stability criteria (as well as the appropriate ad-hoc criterion). Thin solid line segments with a light background indicate equilibrium configurations that are RK1 (and ad-hoc) stable but Bloch wave unstable. Dashed line segments with a light background are "stable" only with respect to the appropriate ad-hoc criterion. Finally, plain dashed line segments are unstable with respect to all the stability criteria considered. We note again that the loading device has no effect on the structure's RK1 and Bloch wave stability. This is because the RK1 and Bloch wave stability criteria consider only perturbations that leave the boundary of an appropriate BVP fixed. Thus, all three principal equilibrium paths become Bloch wave unstable at the same deformation of approximately $\Delta_c = 6.14 \times 10^{-3}$ and RK1 unstable at a deformation of approximately $\Delta = 1.2 \times 10^{-2}$. The Bloch wave instability is the first loss of stability for the
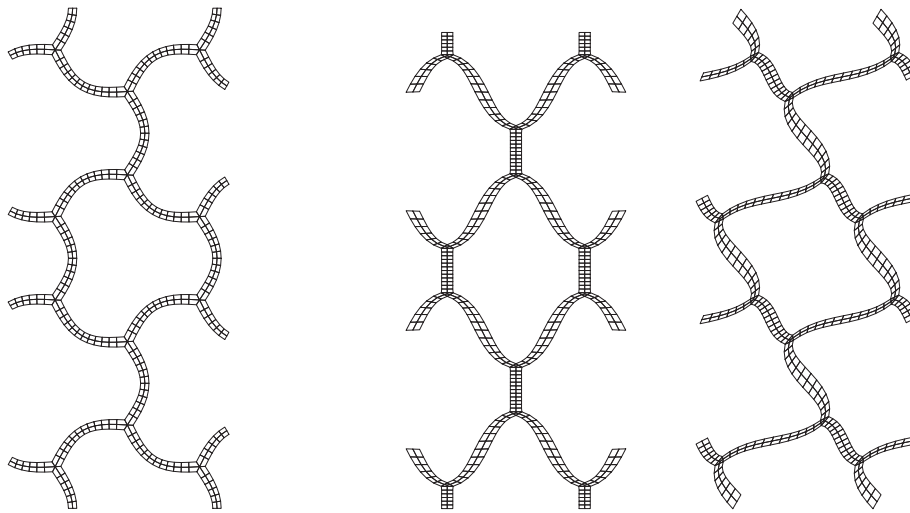
Fig. 15. Primitive unit cell Cauchy–Born bifurcation modes obtained from a two-dimensional plane strain FEM simulation. Left: simple three-fold symmetric bifurcation mode. Right: two two-fold symmetric deformations making up a (symmetry adapted) basis for the double bifurcation point. Multiple copies of the deformed primitive unit cell are shown so as to make the resulting deformation pattern more easily recognizable.

honeycomb under the considered loading conditions. We will return to this first instability when we consider bifurcation from the principal paths in the next subsection. After the principal paths become Bloch wave unstable they each remain RK1 stable for a considerable further amount of deformation.

Finally, we note that the ad-hoc stability criteria, Eqs. (26)–(28), dramatically overestimate the range of stability for all loadings in this situation. However, it is interesting to see that in the live load case the ad-hoc criterion predicts loss of stability at the same deformation as the RK1 criterion.

5.1.2. Principal path Hessian bifurcation points and associated eigenmodes

We now focus on the bifurcation points along the principal path. The open circles with associated numbers in Fig. 13 correspond to Hessian bifurcation points and indicate the number of Hessian eigenvalues that become zero simultaneously.

Starting with the displacement control system, we see that there is a simple bifurcation (one zero Hessian eigenvalue) at the path's loss of ad-hoc stability. Fig. 14 shows the associated deformation mode (eigenvector) on the left. (Here, we have replicated the deformed primitive unit cell so as to make the resulting deformation pattern more easily recognizable.)

We see that the bifurcation mode breaks the rotational symmetry of the honeycomb, reducing it from six-fold to three-fold symmetry. The bifurcation point corresponds to the first Euler buckling load of the hexagonal honeycomb's struts and the deformation pattern of alternating *inward* then *outward* buckling around a single hexagon provides a mechanism that accommodates the rotation of the strut's ends while producing no macroscopic shear deformation ($\delta U_{xy} = 0$). An asymptotic analysis of this bifurcation point reveals that it is a symmetric supercritical bifurcation with a single symmetric (pitchfork) bifurcated path crossing the principal path. Using the techniques described in Section 4.2.2, the bifurcating path's initial post-bifurcation behavior was computed and found to be Bloch wave and RK1 unstable. A typical configuration on this bifurcation path looks just like the mode shown on the left in Fig. 14.

Switching now to the live load control system, we see that the first bifurcation point of its Hessian is a double bifurcation (two zero eigenvalues). A symmetry adapted basis (McWeeny, 2002) for the corresponding two-dimensional eigenvector space is shown, on the right, in Fig. 14. This double bifurcation is seen to break the rotational symmetry of the honeycomb reducing it from six-fold to

two-fold symmetry. An asymptotic analysis of the bifurcation point reveals that it is an asymmetric bifurcation with three (symmetry related) transcritical bifurcated paths crossing the principal path. Using the techniques described in Section 4.2.2, the initial post-bifurcation behavior for one of the three, symmetry related, bifurcating paths was computed and found to be Bloch wave and RK1 unstable. (However, the ad-hoc criterion indicates unstable behavior for the path segment below the bifurcation point, and stable behavior for the path segment above the bifurcation point.) A typical configuration on this bifurcation path looks just like the first of the two modes shown on the right in Fig. 14.

For the dead load control case, we see that the simple bifurcation of the displacement control system and the double bifurcation of the live load control system coalesce to create a triple bifurcation point. Equivariant bifurcation theory (Healey, 1988; Ikeda and Murota, 2010; Vanderbauwhede, 1982) predicts only simple or double bifurcations for a system with six-fold dihedral symmetry. Therefore, the triple bifurcation of the dead load control system is, in this sense, degenerate and an explanation for this degeneracy is necessary. In order for the dead load control system to have a triple bifurcation associated with the three modes shown in Fig. 14, each of these modes must simultaneously represent a *zero-energy mode* for the honeycomb structure. For the left-hand mode to be zero-energy, it must be that the bifurcation point occurs at the first Euler buckling load of the honeycomb's struts. To understand how it is that the two right-hand modes (which are identical up to a rigid rotation) are zero-energy modes, we make the following two observations. First, two struts in each hexagon remain straight and *unperturbed* by the mode; no perturbation means no change in energy. Second, the remaining four struts in each hexagon clearly undergo further deformation as part of the mode, and the only way this can occur with zero energy is if this deformation corresponds to a first Euler buckling mode shape. Indeed, this is what happens, with the four struts deforming so that the rigid joints experience no rotation. However, the deformation just described is not possible without an accompanying macroscopic deformation. A straight forward geometric calculation proves that for an Euler buckling mode amplitude of α, the necessary uniform deformation for the first of the two deformation modes shown on the right-hand side of Fig. 14 is

$$\delta \mathbf{U}(\alpha) = \begin{bmatrix} -4\alpha & 0 \\ 0 & 2\alpha \end{bmatrix}.$$
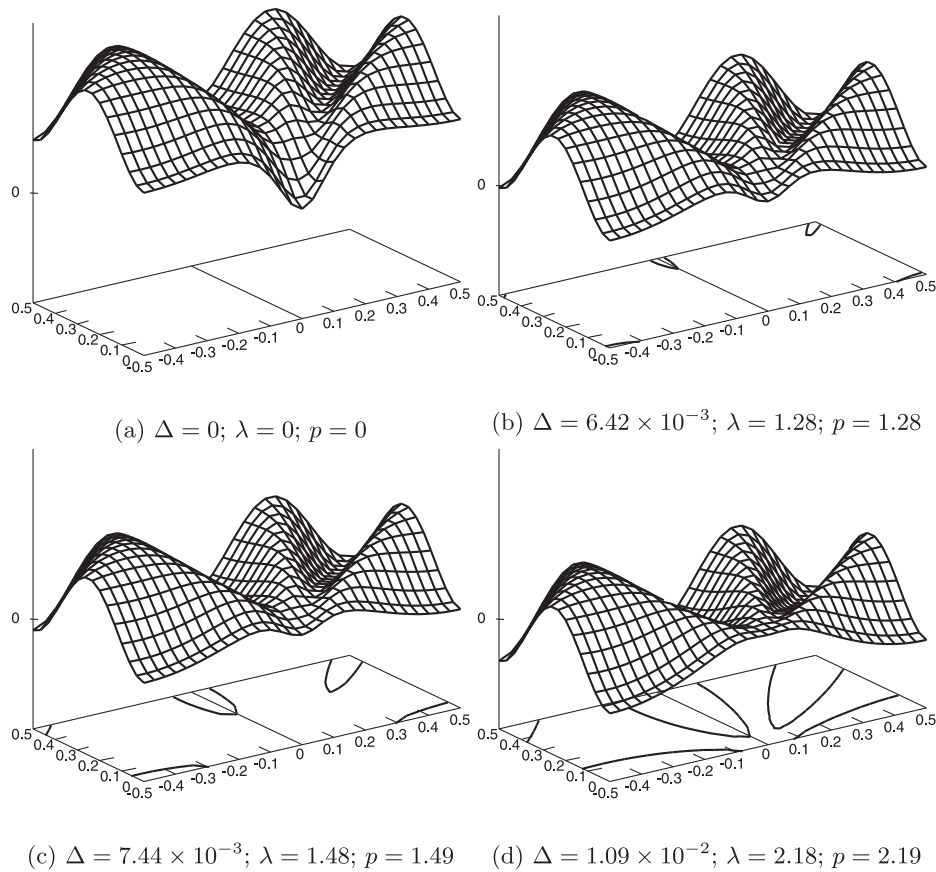
(a) $\Delta = 0$; $\lambda = 0$; $p = 0$

(b) $\Delta = 6.42 \times 10^{-3}$; $\lambda = 1.28$; $p = 1.28$

(c) $\Delta = 7.44 \times 10^{-3}$; $\lambda = 1.48$; $p = 1.49$

(d) $\Delta = 1.09 \times 10^{-2}$; $\lambda = 2.18$; $p = 2.19$

Fig. 16. Minimum Bloch wave eigenvalue $\Lambda^{\dagger}(\mathbf{k})$ surfaces, as a function of the wave vector components k_1 and k_2, for four distinct deformations along the honeycomb's principal equilibrium path.

This uniform deformation perturbation produces a change in area of the honeycomb structure. For the displacement control system this deformation is prohibited by the loading device. For the live load control system, the loading device couples with this deformation and acts to reduce the Hessian eigenvalues associated with such deformations. This results in the double bifurcation occurring at a significantly reduced level of compression for this system. However, for the dead load control system the loading device does not contribute directly to the value of the system's Hessian eigenvalues and the three above described zero-energy modes occur at precisely the same level of compression. The post-bifurcation behavior of this degenerate triple bifurcation point is quite complex. The three-fold symmetric path is easily computed with the methods of Section 4.2.2. However, the two-fold modes now interact with the three-fold mode and the isolated two-fold equilibrium paths degenerate into a two-dimensional manifold of equilibrium configurations. The complete numerical characterization of such an equilibrium manifold requires the use of multi-parameter continuation methods (Allgower and Georg, 2003). However, this is not pursued in this work.

It is interesting to note that the degenerate behavior of the dead load control system just discussed is an artifact of the structural beam model adopted for the description of the hexagon struts and the associated idealization of the honeycomb's rigid joints. Indeed, if two-dimensional plane strain finite elements are used to resolve the continuum deformation of the hexagon struts it is observed that the deformation mechanism near the joints for the two-fold modes is very different than that observed at the strut mid-points for the Euler buckling deformation of the three-fold mode. This is seen in Fig. 15, where the deformation modes of Fig. 14 as computed with a two-dimensional FEM mesh are shown.

This difference in the deformations represents a breaking of an *internal-symmetry* found in the beam-based honeycomb model, and results in a splitting of the triple bifurcation, seen in Fig. 13 for the dead load control system, into separate double and simple bifurcations similar to the live load control system's behavior.

5.1.3. Principal path Bloch wave bifurcation behavior

Having discussed the unit cell Hessian bifurcation behavior for the primitive unit cell equi-biaxial loading of the honeycomb, we next consider the Bloch wave bifurcation behavior. As discussed in Section 4.1.2, the Bloch wave criterion requires all Bloch wave eigenvalues $\Lambda(\mathbf{k}, h)$ to be positive.[12] This criterion first fails to be satisfied when $\Lambda(\mathbf{k}_{cr}, h_{cr}) = 0$ for some $\mathbf{k}_{cr}$ and some h_{cr}. This, in fact, corresponds to a bifurcation and a bifurcated equilibrium path is expected to emerge from the principal path at such a point. However, this is not limited to the first occurrence of a Bloch wave zero eigenvalue. Indeed, every equilibrium configuration for which there exists a Bloch wave zero eigenvalue corresponds to a *Bloch wave* bifurcation point. As will be discussed below, the wave vector $\mathbf{k}_{cr}$ associated with such a Bloch wave bifurcation point is intimately connected with the translational periodicity of the corresponding Bloch wave bifurcation deformation mode.

In order to explore the Bloch wave bifurcation behavior of the honeycomb structure subjected to equi-biaxial compressive loading, we first recall that since the Bloch wave criterion does not consider macroscopic uniform deformation of the structure, the loading device has no direct effect on the Bloch wave eigenvalues or eigenvectors. Thus, the Bloch wave bifurcation behavior for

---

[12] Recall the special case of $\mathbf{k} = \mathbf{0}$ discussed in Footnote [9].
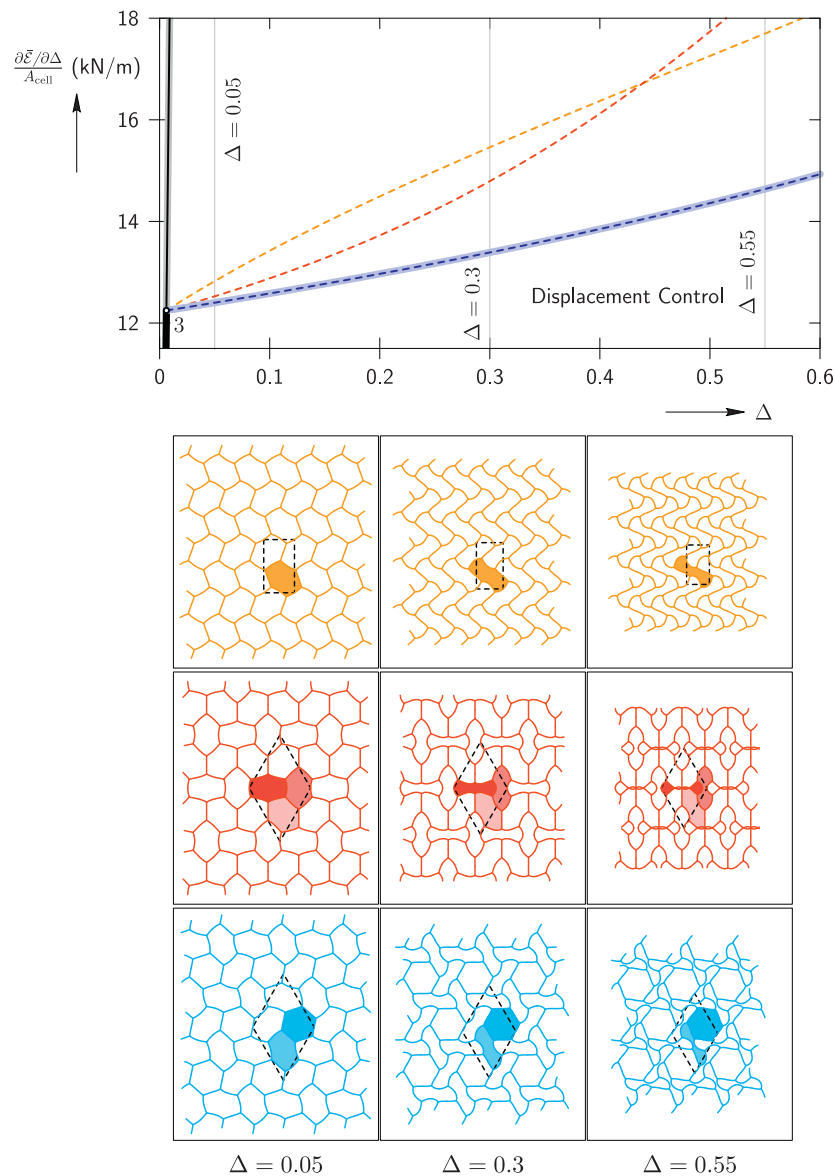
Fig. 17. Displacement control bifurcation diagram and deformed configurations associated with the triple Bloch wave bifurcation of the hexagonal honeycomb structure. The bifurcation diagram shows Mode I (orange), Mode II (red), and Mode III (blue) equilibrium paths. All three modes are found to be unstable with respect to the RK1 and Bloch wave criteria. In contrast, the ad-hoc criterion predicts that Mode III is stable. The deformed equilibrium configuration at three loading parameters ($\Delta = 0.05$, 0.3, and 0.55) is shown for Mode I (first row), Mode II (second row) and, Mode III (third row). (For interpretation of the references to color in this figure legend, the reader is referred to the web version of this article.)

each of our three loading devices is identical for the hexagonal principal equilibrium path. One useful way to visualize the Bloch wave eigenvalues is to only consider the minimum eigenvalue for each wave vector: $\Lambda^{\dagger}(\mathbf{k}) \equiv \min_h \Lambda(\mathbf{k}, h)$. This set of minimum eigenvalues is capable of capturing the first instability associated with each independent wave vector and can be plotted as a two-dimensional surface over the first BZ within reciprocal space. Fig. 16 shows the $\Lambda^{\dagger}$ surface at four distinct deformations along the honeycomb's principal equilibrium path.

In Fig. 16a the eigenvalue surface for the undeformed configuration is shown. Fig. 16b shows the surface for a configuration just after the first Bloch wave bifurcation is encountered. The contour lines on the plot's basal plane are zero-eigenvalue curves of the eigenvalue surface. We see that the first Bloch wave bifurcation occurs simultaneously for three[13] BZ boundary

wave vectors, $(k_1, k_2) = (0, 1/2)$, $(k_1, k_2) = (1/2, 0)$, and $(k_1, k_2) = (1/2, 1/2)$. These vectors are represented in Fig. 16 (see also, Fig. 11). These three wave vectors are symmetry related by the six-fold rotational symmetry of the hexagonal honeycomb structure. As the deformation continues to increase, we see in Fig. 16c and d that the region of unstable Bloch wave modes (negative eigenvalues) propagates along the high-symmetry directions toward the $\mathbf{k} = \mathbf{0}$ point (the so-called Γ-point) in reciprocal space. Thus, every equilibrium configuration following the initial Bloch wave bifurcation, along the structure's principal equilibrium path, is also a Bloch wave bifurcation point.

Generally, points near the BZ boundary of reciprocal space (as indicated in Fig. 11) can be associated with short (small multiples of the principal path translational periodicity) wavelength Bloch

---

[13] Note that, although the Bloch wave eigenvalues for $(k_1, k_2) = (0, -1/2)$, $(-1/2, 0)$, and $(-1/2, -1/2)$ also become zero, these three wave vectors are not

independent from the first three since they are related to them by integer multiples of the reciprocal lattice vectors and are, thus, technically not part of the first BZ.
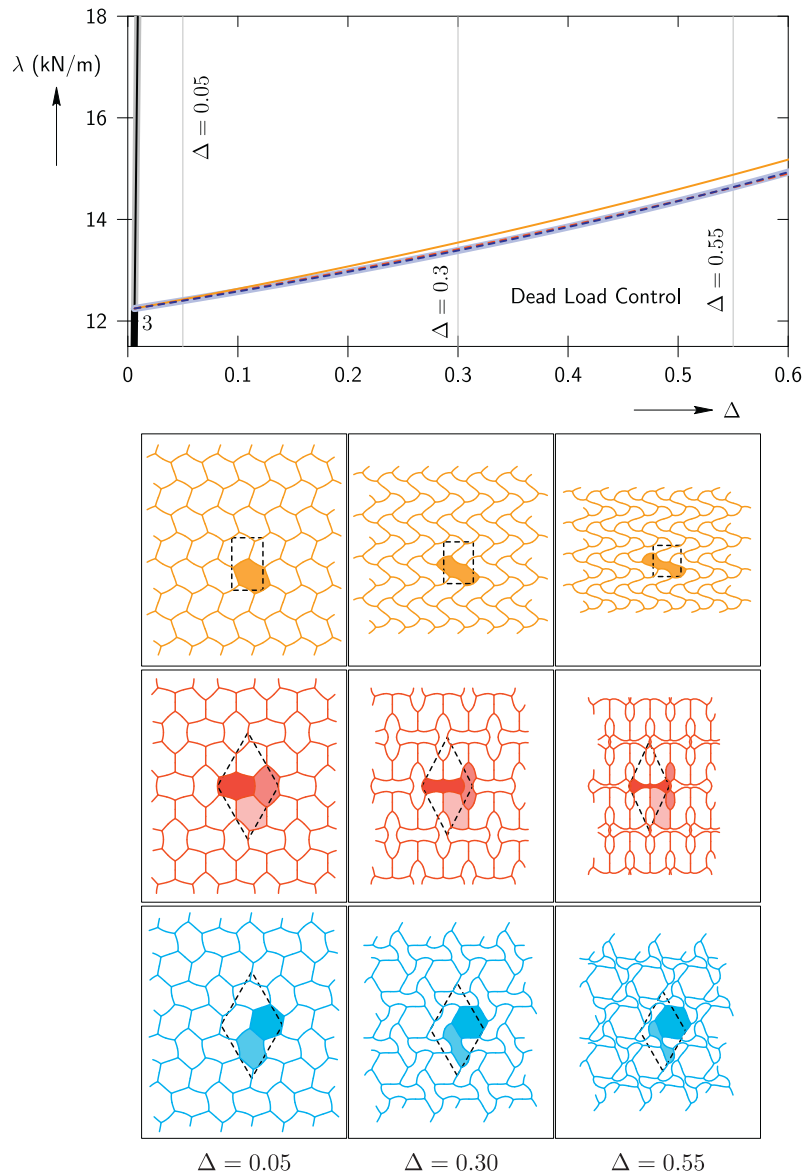
Fig. 18. Dead load control bifurcation diagram and deformed configurations associated with the triple Bloch wave bifurcation of the hexagonal honeycomb structure. The bifurcation diagram shows Mode I (orange), Mode II (red), and Mode III (blue) equilibrium paths. Mode I is RK1 stable but Bloch wave (and ad-hoc) unstable and is indicated with a thin solid line segment. Mode II and Mode III are unstable with respect to both the RK1 and Bloch wave criteria. However, the ad-hoc criterion predicts that Mode III is stable. The deformed equilibrium configuration at three loading parameters ($\Delta = 0.05$, 0.3, and 0.55) is shown for Mode I (first row), Mode II (second row), and Mode III (third row). (For interpretation of the references to color in this figure legend, the reader is referred to the web version of this article.)

wave perturbations, and points near the Γ-point can be associated with long (large multiples of the principal path translational periodicity) wavelength Bloch wave perturbations. In the limit, as the zero-eigenvalue curves reach the Γ-point, RK1 stability is lost and a macroscopic loss of strong ellipticity occurs. Thus, we see that the RK1 stability criterion is a special case of the Bloch wave criterion corresponding to a loss of Bloch wave stability of the Bloch wave acoustic eigenvalues for wave vectors of infinitesimal magnitude (i.e., **k** vectors in the neighborhood of the Γ-point). See also Fig. 12.

Each wave vector **k** is associated, via the Bloch theorem Eq. (24), with a plane wave deformation perturbation characterized by a set of lattice planes (identified by the direction of the wave vector) and a periodic repeat distance measured perpendicular to the lattice planes. In order to describe these perturbations within the Cauchy–Born Kinematic framework used here, an appropriate unit cell must be identified. For a given set of wave vectors with ratio-

nal components (k_1, k_2), Sorkin et al. (2014) describe a procedure, which they call the Cascading Cauchy–Born (CCB) algorithm, that produces the smallest unit cell capable of describing all of the associated Bloch wave perturbations.

In order to explore the first Bloch wave bifurcation point, we apply the Cascading Cauchy–Born algorithm to the corresponding wave vectors. When applied, individually, to the wave vectors $(k_1, k_2) = (0, 1/2)$, $(1/2, 1/2)$, and $(1/2, 0)$, the algorithm identifies the 1×2 unit cell at the top-middle, middle-middle, and bottom-middle of Fig. 9, respectively. If any two or more of these wave vectors are used as input to the CCB algorithm, it identifies the 2×2 unit cell at the right of Fig. 9.

5.2. 1×2 unit cell bifurcated equilibrium paths and their stability

Using the 1×2 unit cell at the middle-middle of Fig. 9 we find that first Bloch wave bifurcation point identified in the
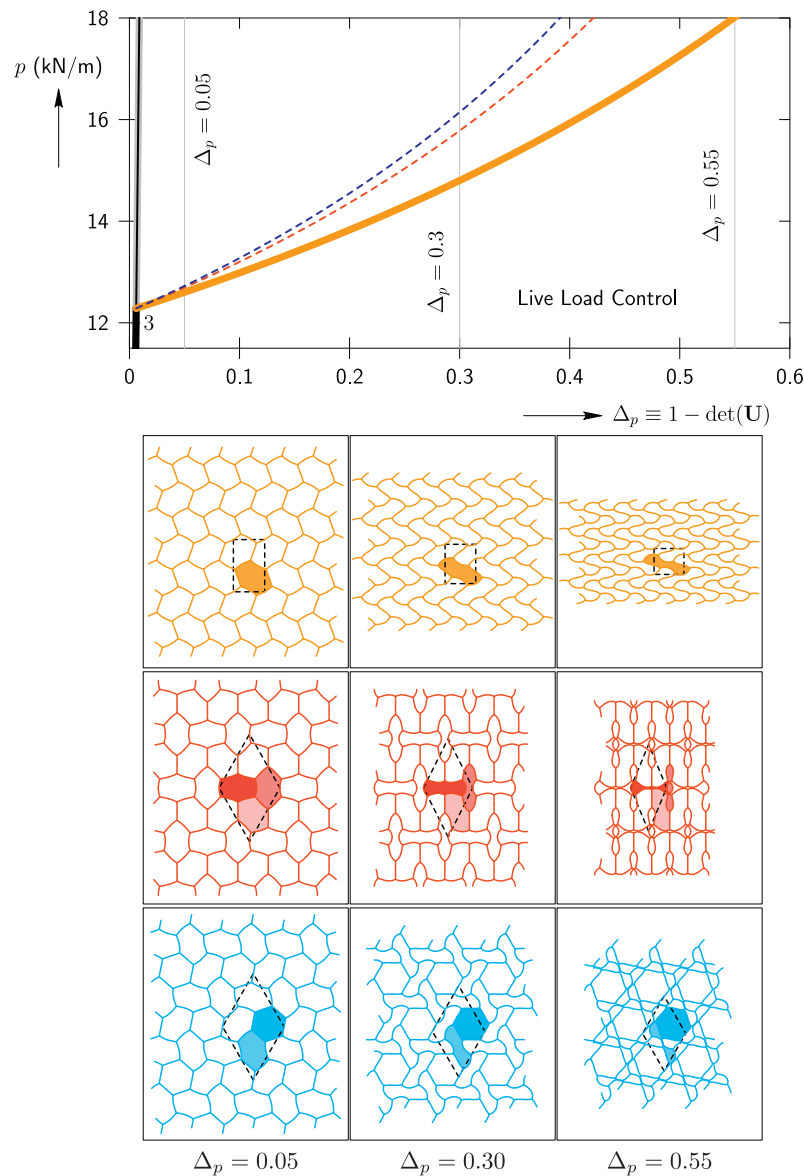
Fig. 19. Live load control bifurcation diagram and deformed configurations associated with the triple Bloch wave bifurcation of the hexagonal honeycomb structure. The bifurcation diagram shows Mode I (orange), Mode II (red), and Mode III (blue) equilibrium paths. Mode I is RK1 and Bloch wave stable (as well as ad-hoc stable). Mode II and Mode III are unstable with respect to both the RK1 and Bloch wave criteria (and the ad-hoc criterion). The deformed equilibrium configuration at three loading parameters ($\Delta_p = 0.05$, 0.3, and 0.55) is shown for Mode I (first row), Mode II (second row), and Mode III (third row). (For interpretation of the references to color in this figure legend, the reader is referred to the web version of this article.)

previous section (using the primitive unit cell shown on the left in Fig. 9) becomes a simple Hessian bifurcation point with a single Hessian eigenvalue going to zero at $\Delta_c \approx 0.006$. The branch-following techniques described in Section 4.2.1 were used to numerically compute the post-bifurcation behavior of the single bifurcating path. The branch is identified as the Mode I pattern found in previous studies. For each of the 1×2 unit cells shown in the middle of Fig. 9, we obtain one of the symmetry related variants of the Mode I deformation pattern. The equilibrium path for each loading condition is shown in orange in the bifurcation diagrams of Figs. 17–19. The corresponding Mode I deformation patterns at three different loading parameter values are shown in the first row of these figures. We see that the loading conditions have a significant effect on the Mode I equilibrium path and its stability. Displacement control requires uniform dilatation and results in all of the stability criteria being violated for the Mode I solution. Dead load control allows the structure to undergo significantly more compression in the vertical direction. This results in the Mode I so-

lution becoming stable with respect to the RK1 criterion. However, it is found to be unstable with respect to the Bloch wave criterion (and the ad-hoc criterion). Here, stability with respect to the RK1 criterion only is indicated by the thin solid line segment. These stability properties are due to the existence of negative Bloch wave optic eigenvalues for wave vectors in a neighborhood of the Γ-point associated with deformations that vary on the same spatial scale as the 1×2 unit cell. For live load control Mode I is found to be stable with respect to both the RK1 and Bloch wave criteria (as well as the ad-hoc criterion).

5.3. 2×2 unit cell bifurcated equilibrium paths and their stability

Having found all bifurcated equilibrium paths associated with the 1×2 cells, we next considered the 2×2 cell shown on the right in Fig. 9. This cell incorporates all of the Bloch wave deformation modes associated with the first Bloch wave bifurcation point identified in Section 5.1.3. Therefore, that point
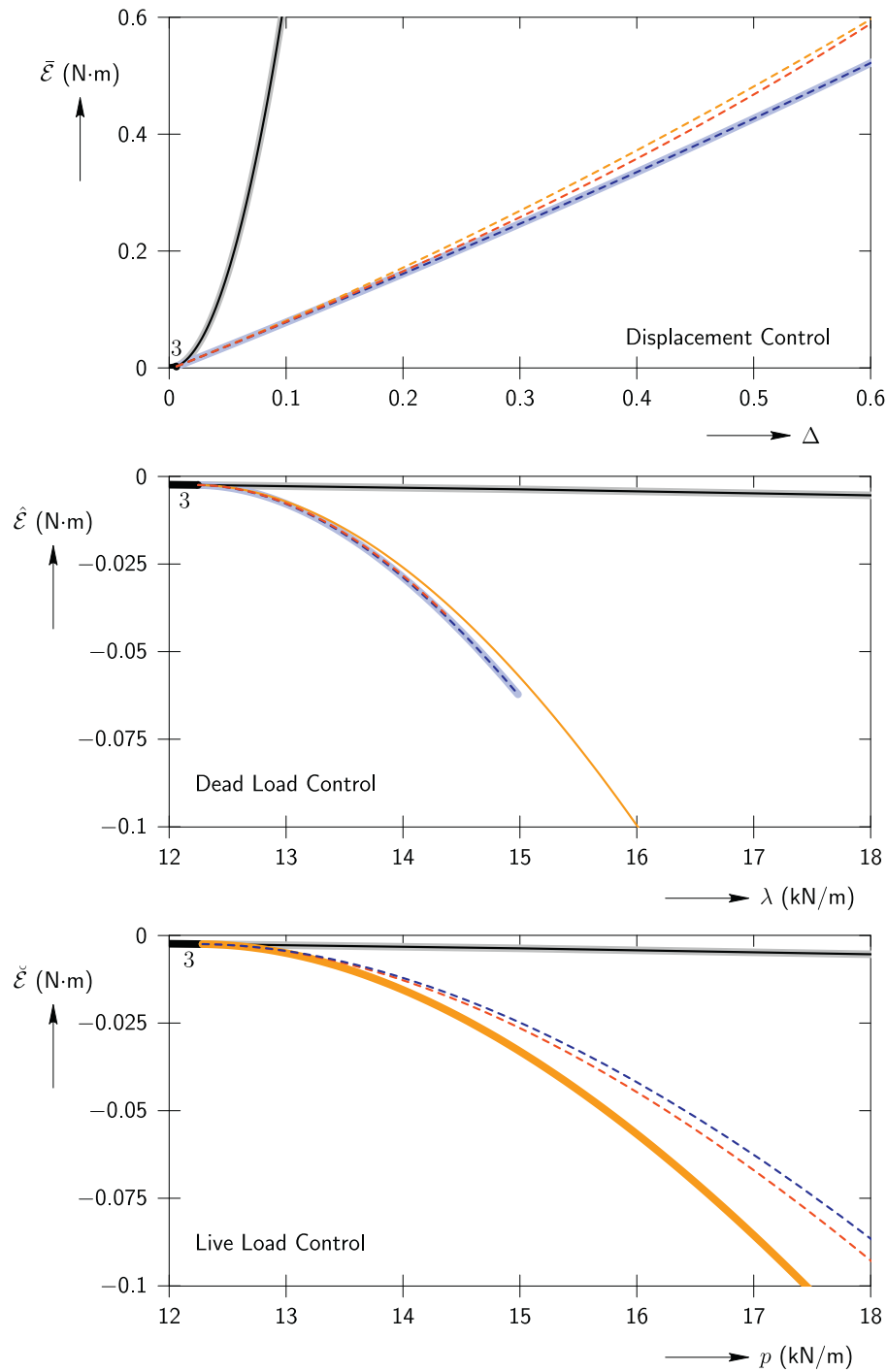
Fig. 20. Energy versus loading parameter diagrams for displacement (top), dead load (middle), and live load (bottom) control conditions. Mode I is shown in orange, Mode II in red, and Mode III in blue. The stability of each path segment is indicated by the line type as described in the text. (For interpretation of the references to color in this figure legend, the reader is referred to the web version of this article.)

becomes a triply degenerate Hessian bifurcation point with three Hessian eigenvalues going to zero at $\Delta_c \approx 0.006$. The bifurcation and branch-following techniques of Section 4.2 were used to numerically compute the post-bifurcation behavior of all bifurcating paths. These consist of three sets of symmetry related modes: three Mode I paths computed using the 1×2 unit cells and discussed in the previous subsection;[14] six Mode II paths;

and four Mode III paths. The equilibrium paths, for each loading condition, associated with Mode II (red) and Mode III (blue) are shown in the bifurcation diagrams of Figs. 17–19. The corresponding deformation patterns at three different loading parameter values are shown in the second (Mode II) and third (Mode III) rows of these figures. Again, we see that the loading conditions have a significant effect on the equilibrium paths and their stability. Mode II and Mode III are found to be RK1 and Bloch wave unstable for all loadings. However, the ad-hoc stability criterion predicts that Mode III is stable for displacement and dead load control conditions.

---

[14] These paths need not actually be recomputed, as group theory arguments can be used to prove that the previously found solutions are identical to the corresponding solutions for the 2×2 unit cell.
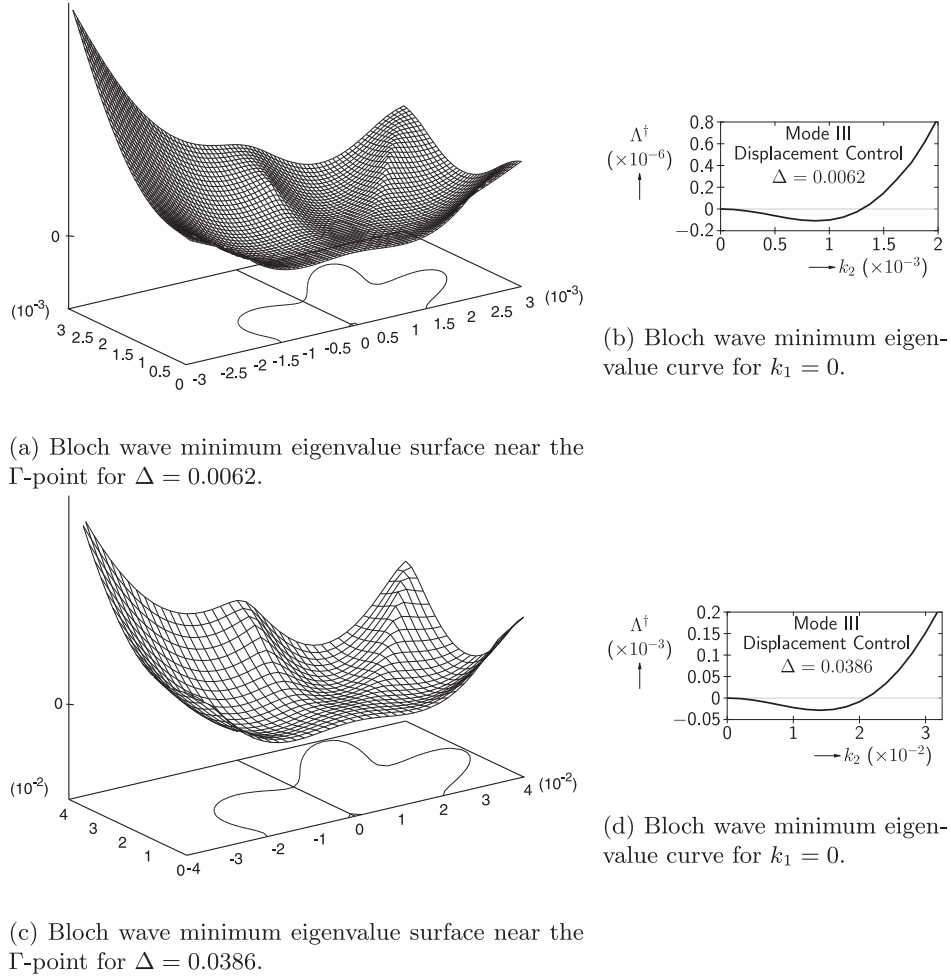
(b) Bloch wave minimum eigen-
value curve for $k_1 = 0$.

(a) Bloch wave minimum eigenvalue surface near the
Γ-point for $\Delta = 0.0062$.

(d) Bloch wave minimum eigen-
value curve for $k_1 = 0$.

(c) Bloch wave minimum eigenvalue surface near the
Γ-point for $\Delta = 0.0386$.

Fig. 21. Bloch wave minimum eigenvalue surfaces near the Γ-point, for the displacement control bifurcated equilibrium Mode III path. Note the significantly different scales used for the axes of the graphs. (Top: $\Delta = 0.0062$) Almost immediately after bifurcation there exist long wavelength Bloch wave modes (with $|\mathbf{k}| < 2.5 \times 10^{-3}$) that are unstable. (Bottom: $\Delta = 0.0386$) Somewhat later in the post-bifurcation evolution the domain of unstable long wavelength Bloch wave modes ($|\mathbf{k}| < 4.0 \times 10^{-2}$) has increased in size by more than an order of magnitude.

To further understand the relationships between the three bifurcated equilibrium modes of deformation, the unit cell energy function has been plotted as a function of the loading parameter for each of the loading conditions in Fig. 20.

For the displacement control case the energy $\bar{\mathcal{E}}$ includes only the unit cell strain energy which increases as the boundary displacements are changed. However, for the dead load and live load control cases the energy, $\hat{\mathcal{E}}$ and $\check{\mathcal{E}}$, respectively, includes both the unit cell energy and the loading device energy. The energy of the loading device decreases more rapidly than the strain energy increases during the deformation which leads to negative values. From these figures we see that the ad-hoc stability criterion predicts the lowest total energy equilibrium configuration from those available, even if it does not manage to correctly identify the material stability of the mode.

Finally, we take a special look at the Bloch wave stability of the Mode III equilibrium path. Although we have already noted that Mode III is RK1 and Bloch wave unstable for all loading conditions, a more detailed inspection of the Mode III Bloch wave eigenvalue surface allows for a new insight into its stability properties.

Fig. 21 shows the displacement control Mode III minimum Bloch wave eigenvalue $\Lambda^{\dagger}$ surface for $\mathbf{k}$ near the Γ-point. The surfaces correspond to post-bifurcation equilibrium configurations im-

mediately after bifurcation (at $\Delta = 0.0062$) and somewhat later in the post-bifurcation evolution (at $\Delta = 0.0386$). The remainder of the $\Lambda^{\dagger}$ surface, which is not shown, is found to be above zero (stable). Thus, we see that the displacement control Mode III solution is unstable with respect to long wavelength acoustic Bloch wave modes (as also indicated by the failure of the RK1 criterion). However, we note that this is true only for $\mathbf{k}$ in a very small neighborhood of the Γ-point. The domain of unstable wave vectors is approximately $|\mathbf{k}| < 2.5 \times 10^{-3}$ almost immediately after bifurcation, at $\Delta = 0.0062$, and increases to $|\mathbf{k}| < 4.0 \times 10^{-2}$, at $\Delta = 0.0386$. This means that these two Mode III equilibrium states (with post-bifurcation amplitude $\Delta - \Delta_c = 0.0001$ and 0.0325, respectively) are unstable for very long wavelength perturbations (longer than about 400 and 25 primitive hexagonal unit cells, respectively) but are stable for short and moderate wavelength perturbations. These results are consistent with those of Okumura et al. (2004). These authors found that large unit cells of size 18×18, 16×16 and 14×14 loose stability (in sequence) as the post-bifurcation amplitude increases along the Mode III bifurcated equilibrium path. Here, we demonstrate that these results are a special case of the general trend which can be stated as follows: the post-bifurcation amplitude at which stability is lost scales inversely with the size of the unit cell. We will comment further on this result and its relation to the experiments of Papka and Kyriakides (1999a) in Section 6.
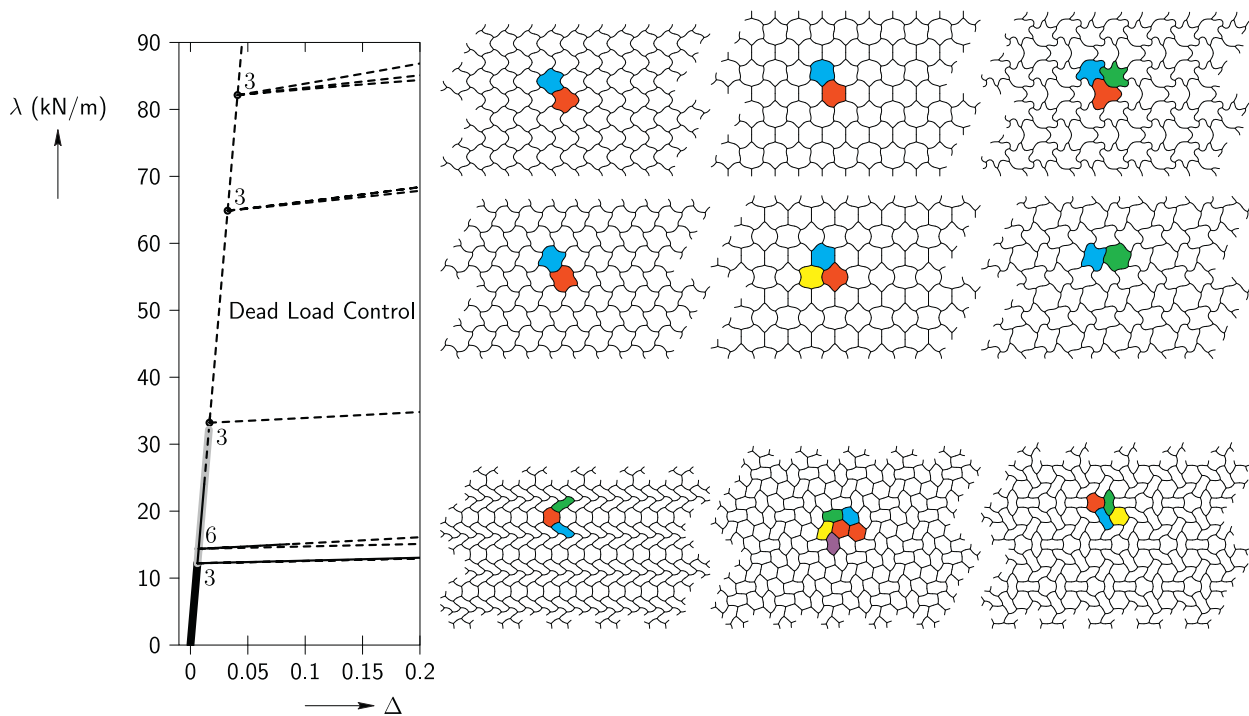
Fig. 22. Bifurcation diagram and additional bifurcated equilibrium configurations for the honeycomb structure. The first triple bifurcation at $\lambda \approx 12$ is a 2×2 unit cell bifurcation point with bifurcating Mode I, Mode II, and Mode III paths as depicted in Fig. 18. The sextuple bifurcation at $\lambda \approx 15$ is a 3×3 unit cell bifurcation with bifurcating paths corresponding to the bottom row of configurations shown to the right. The second triple bifurcation at $\lambda \approx 33$ is the degenerate bifurcation point for the dead load control case identified in Fig. 13 with bifurcating paths similar to the modes shown in Fig. 14. The third triple bifurcation at $\lambda \approx 65$ is a 2×2 unit cell bifurcation with bifurcating paths corresponding to the middle row of configurations shown to the right. Finally, the fourth triple bifurcation at $\lambda \approx 82$ is a 2×2 bifurcation with bifurcating paths corresponding to the top row of configurations shown to the right. Each new configuration is unstable, but the equilibrium deformation patterns are quite interesting. The first two rows can be thought of as *higher-order* versions of the Mode I, Mode II, and Mode III deformations. The third row can be thought of as *mixtures* of various 1×1, 1×2, and 2×2 deformation patterns.

5.4. Additional 2×2 and 3×3 unit cell bifurcated equilibrium configurations

In the interest of further developing our group theory based techniques for performing bifurcation and branch-following simulations, we have also pursued the study of additional Bloch wave bifurcation points found along the principal equilibrium path of the hexagonal honeycomb structure. Here, we will provide only a brief discussion of the type of results that we are able to obtain. In particular, we explored two additional bifurcation points found using the 2×2 unit cell and the first Bloch wave bifurcation point associated with a 3×3 unit cell. The resulting bifurcation diagram and deformed configurations are shown in Fig. 22.

All of the newly obtained bifurcated equilibrium paths are found to be unstable; however the equilibrium deformation patterns obtained are new and quite interesting. The first two rows of configurations shown on the right in the figure correspond to 2×2 unit cell bifurcated paths. If the Mode I, Mode II, and Mode III equilibrium paths of Figs. 17–19 are thought of as deformation patterns associated with *first-order* Euler buckling of the hexagonal struts, then the deformation patterns in the first two rows of Fig. 22 may be thought of as *higher-order* versions of those in Figs. 17–19, where higher-order Euler buckling of the hexagon struts are involved. The third row of Fig. 22 corresponds to the bifurcated equilibrium configurations that emerge from the first Bloch wave bifurcation point associated with a 3×3 unit cell. These deformation patterns are the first to show the possibility of a *mixture* of different equilibrium patterns. For example, the first pattern in the third row of Fig. 22 is a mixture of the 1×1 unit cell deformation mode shown on the left in Fig. 14 and the 1×2 unit cell deformation Mode I shown in Figs. 17–19. The middle

pattern in the third row of Fig. 22 is a *double* Mode III pattern with two undistorted hexagons surrounded by the *flower* pattern. Finally, the third pattern in the third row of Fig. 22 is a *mixture* of the 1×1 unit cell deformation mode shown on the left in Fig. 14 and the 2×2 unit cell deformation Mode II shown in Figs. 17–19.

6. Conclusions

In this work we have revisited the problem of in-plane equibiaxial compression of a regular hexagonal honeycomb structure. We extensively reviewed the existing literature: from the seminal experiments of Papka and Kyriakides (1994); 1999a), to the characterization of the onset of failure by Triantafyllidis and Schraad (1998) and Ohno et al. (2002), to the study of honeycomb postbifurcation behavior using an intuitive approach by Okumura et al. (2002) and the more systematic group-theory methods used by Saiki et al. (2005). Our literature review identified two open theoretical questions about the post-bifurcation behavior of honeycombs: (i) How does the mechanical response of the honeycomb depend on the applied loading device? and (ii) What can the *Bloch wave representation* of all bounded perturbations contribute to our understanding of the stability of post-bifurcated equilibrium configurations?

Our investigation paid special attention to the effects of the loading device on the post-bifurcation and stability behavior. We considered the equilibrium and bifurcation behavior of the infinite perfect hexagonal honeycomb structure subjected to (i) displacement, (ii) dead load (Biot), and (iii) live load (*two-dimensional pressure*) control. We adopted a purely elastic model and employed a linearly elastic material constitutive response. Based on the results of Triantafyllidis and Schraad (1998), the (initial) post-bifurcation

equilibrium and stability behavior predicted by our model is applicable to all real hexagonal geometry honeycomb structures composed of rate-independent solids subjected to equi-biaxial compressive loadings.

We used a systematic branch-following and bifurcation technique for the perfect structure, complemented by analytical group theory results to identify and compute the bifurcation and post-bifurcation behavior of a perfect hexagonal honeycomb structure. An important feature of this methodology is that it does not use the imperfection method. (The imperfection method is a simple heuristic numerical method encountered in engineering practice that often works well for the study of bifurcation behavior associated with equilibrium paths with widely separated bifurcation points. However, the method is highly unreliable for problems with a high degree of symmetry.) For the evaluation of an equilibrium configuration's stability, we employed only strictly necessary stability conditions that are applicable to all boundary value problems. In particular, we used the Rank-One Convexity (RK1) criterion (to evaluate stability with respect to long wavelength perturbations) and the Bloch wave criterion (to evaluate stability with respect to all bounded perturbations).

Using these techniques, we obtained the equilibrium, stability, and bifurcation behavior of the honeycomb subjected to equi-biaxial in-plane compression and identified an infinite set of bifurcation points along this equilibrium path. We investigated the 1×1 unit cell bifurcation behavior of the honeycomb and identified an interesting mathematical degeneracy associated with the use of a structural beam theory to model the struts of the honeycomb structure. We subsequently looked at the 1×2 and 2×2 unit cell bifurcation behavior of the honeycomb and confirmed previous results from the literature. However, we went further in our study of the post-bifurcation behavior and identified the stability of each equilibrium path relative to the RK1 and Bloch wave stability criteria. We also identified a common but *ad-hoc* energy based stability criterion (that is not generally necessary for all boundary value problems). We showed that in many cases the ad-hoc criterion provides erroneous predictions. Finally, we obtained a few representative and interesting examples of previously unreported equilibrium configurations associated with 2×2 and 3×3 unit cells.

Our results confirmed that the Mode III flower pattern obtained under displacement control conditions is RK1 unstable (as first reported by Okumura et al., 2002, but unfortunately dismissed by these authors). Further, we used the Bloch wave stability criterion to gain a deeper understanding of the stability properties of the Mode III bifurcated equilibrium path. We found that although this mode is unstable with respect to very long wavelength perturbations, it is stable with respect to short and moderate wavelength perturbations. This provides an explanation for how (Papka and Kyriakides, 1999a) were able to observe this mode: the 18×21 unit cell specimens used in their experiments were well within the Mode III moderate wavelength stability range identified in this work.

Acknowledgments

References

Allgower, E.L., Georg, K., 2003. Introduction to Numerical Continuation Methods. Volume 45 of Classics in Applied Mathematics. SIAM.

Chillingworth, D., Marsden, J., Wan, Y., 1982. Symmetry and bifurcation in three-dimensional elasticity, part I. Arch. Ration. Mech. Anal. 80, 295–331. doi:10.1007/BF00253119.

Chillingworth, D., Marsden, J., Wan, Y., 1983. Symmetry and bifurcation in three-dimensional elasticity. part II. Arch. Ration. Mech. Anal. 83, 363–395. doi:10.1007/BF00963840.

Como, M., Grimaldi, A., 1995. Theory of Stability of Continuous Elastic Structures. Library of Engineering Mathematics. CRC Press.

Dobson, M., Elliott, R.S., Luskin, M., Tadmor, E.B., 2007. A multilattice quasi-continuum for phase transforming materials: cascading Cauchy–Born kinematics. J. Computer-Aided Mater. Des. 14 (Suppl. 1), S219–S237. doi:10.1007/s10820-007-9084-7.

Dobson, M., Elliott, R.S., Tadmor, E.B., 2006. A quasicontinuum for complex crystals. In: Gumbsch, P. (Ed.), Proceedings of the Third International Conference on Multiscale Materials Modeling. Freiburg, Germany, pp. 889–896.

Dove, M.T., 1993. Introduction to Lattice Dynamics. Cambridge University Press.

Elliott, R.S., 2007. Multiscale bifurcation and stability of multilattices. J. Computer-Aided Mater. Des. 14 (Suppl. 1), S143–S157. doi:10.1007/s10820-007-9075-8.

Elliott, R.S., Shaw, J.A., Triantafyllidis, N., 2006a. Stability of crystalline solids—II: application to temperature-induced martensitic phase transformations in bi-atomic crystals. J. Mech. Phys. Solids 54 (1), 193–232. doi:10.1016/j.jmps.2005.07.008.

Elliott, R.S., Triantafyllidis, N., Shaw, J.A., 2006b. Stability of crystalline solids—I: continuum and atomic-lattice considerations. J. Mech. Phys. Solids 54 (1), 161–192. doi:10.1016/j.jmps.2005.07.009.

Elliott, R.S., Triantafyllidis, N., Shaw, J.A., 2011. Reversible stress-induced martensitic phase transformations in a bi-atomic crystal. J. Mech. Phys. Solids 59 (2), 216–236. doi:10.1016/j.jmps.2010.10.011.

Geymonat, G., Muller, S., Triantafyllidis, N., 1993. Homogenization of nonlinearly elastic materials, microscopic bifurcation and macroscopic loss of rank-one convexity. Arch. Ration. Mech. Anal. 122, 231–290. doi:10.1007/BF00380256.

Gibson, L.J., Ashby, M.F., 1997. Cellular Solids, second edition Cambridge University Press.

Gong, L., Kyriakides, S., Triantafyllidis, N., 2005. On the stability of Kelvin cell foams under compressive loads. J. Mech. Phys. Solids 53 (4), 771–794.

Healey, T.J., 1988. A group-theoretic approach to computational bifurcation problems with symmetry. Comput. Methods Appl. Mech. Eng. 67 (3), 257–295. doi:10.1016/0045-7825(88)90049-7.

Heinz, H.-P., Kpper, T., Stuart, C., 1992. Existence and bifurcation of solutions for nonlinear perturbations of the periodic Schrodinger equation. J. Differ. Equ. 100 (2), 341–354. http://dx.doi.org/10.1016/0022-0396(92)90118-7.

Ikeda, K., Murota, K., 2010. Imperfect Bifurcation in Structures and Materials: Engineering Use of Group-Theoretic Bifurcation Theory. Volume 149 of Applied Mathematical Sciences, second edition, Springer.

Jusuf, V., 2010. Algorithms for Branch-Following and Critical Point Identification in the Presence of Symmetry (Master's thesis). Department of Aerospace Engineering and Mechanics, The University of Minnesota, Minneapolis, Minnesota, USA.

Jusuf, V., 2013. A New Framework for the Interpretation of Modulated Martensites in Shape-Memory Alloys (Ph.D. thesis). Department of Aerospace Engineering and Mechanics, The University of Minnesota, Minneapolis, Minnesota, USA.

Laroussi, M., Sab, K., Alaoui, A., 2002. Foam mechanics: nonlinear response of an elastic 3d-periodic microstructure. Int. J. Solids Struct. 39 (13–14), 3599–3623. http://dx.doi.org/10.1016/S0020-7683(02)00172-5.

Liu, J., Bertoldi, K., 2015. Bloch wave approach for the analysis of sequential bifurcations in bilayer structures. Proc. R. Soc. Lond. A: Math. Phys. Eng. Sci. 471 (2182). doi:10.1098/rspa.2015.0493.

McWeeny, R., 2002. Symmetry: An Introduction to Group Theory and Its Applications. Dover.

Michailidis, P., Triantafyllidis, N., Shaw, J., Grummon, D., 2009. Superelasticity and stability of a shape memory alloy hexagonal honeycomb under in-plane compression. Int. J. Solids Struct. 46 (13), 2724–2738. http://dx.doi.org/10.1016/j.ijsolstr.2009.03.013.

Michel, J., Lopez-Pamies, O., Castaneda, P.P., Triantafyllidis, N., 2007. Microscopic and macroscopic instabilities in finitely strained porous elastomers. J. Mech. Phys. Solids 55 (5), 900–938. http://dx.doi.org/10.1016/j.jmps.2006.11.006.

Ohno, N., Okumura, D., Noguchi, H., 2002. Microscopic symmetric bifurcation condition of cellular solids based on a homogenization theory of finite deformation. J. Mech. Phys. Solids 50 (5), 1125–1153. doi:10.1016/S0022-5096(01)00106-5.

Okumura, D., Ohno, N., Noguchi, H., 2002. Post-buckling analysis of elastic honeycombs subject to in-plane biaxial compression. Int. J. Solids Struct. 39 (13-14), 3487–3503. doi:10.1016/S0020-7683(02)00165-8.

Okumura, D., Ohno, N., Noguchi, H., 2004. Elastoplastic microscopic bifurcation and post-bifurcation behavior of periodic cellular solids. J. Mech. Phys. Solids 52 (3), 641–666. doi:10.1016/j.jmps.2003.07.002.

Papka, S., Kyriakides, S., 1994. In-plane compressive response and crushing of honeycomb. J. Mech. Phys. Solids 42 (10), 1499–1532.

Papka, S., Kyriakides, S., 1998. Experiments and full-scale numerical simulations of in-plane crushing of a honeycomb. Acta Mater. 46 (8), 2765–2776. doi:10.1016/S1359-6454(97)00453-9.

Papka, S., Kyriakides, S., 1999a. Biaxial crushing of honeycombs—part I: experiments. Int. J. Solids Struct. 36 (29), 4367–4396. doi:10.1016/S0020-7683(98)00224-8.

Papka, S., Kyriakides, S., 1999b. Biaxial crushing of honeycombs—part II: analysis. Int. J. Solids Struct. 36 (29), 4397–4423. doi:10.1016/S0020-7683(98)00225-X.

Pattamatta, S., Elliott, R.S., Tadmor, E.B., 2014. Mapping the stochastic response of nanostructures. Proc. Natl. Acad. Sci. USA 111 (17), E1678–E1686. doi:10.1073/pnas.1402029111.

Saiki, I., Ikeda, K., Murota, K., 2005. Flower patterns appearing on a honeycomb structure and their bifurcation mechanism. Int. J. Bifurc. Chaos 15 (02), 497–515. doi:10.1142/S021812740501217X.

Saiki, I., Terada, K., Ikeda, K., Hori, M., 2002. Appropriate number of unit cells in a representative volume element for micro-structural bifurcation encountered in a multi-scale modeling. Comput. Methods Appl. Mech. Eng. 191 (23–24), 2561–2585. doi:10.1016/S0045-7825(01)00413-3.

Sorkin, V., Elliott, R.S., Tadmor, E.B., 2014. A local quasicontinuum for 3D multilattice crystalline materials: Application to shape-memory alloys. Model. Simul. Mater. Sci. Eng. 22, 055001-1–055001-22. doi:10.1088/0965-0393/22/5/055001.

Tadmor, E.B., Miller, R.E., Elliott, R.S., 2012. Continuum Mechanics and Thermodynamics: From Fundamental Concepts to Governing Equations, first edition, Cambridge University Press.

Taylor, R. L., 2011. FEAP – finite element analysis program, version 8.3. University of California, Berkeley. http://www.ce.berkeley/feap.

Triantafyllidis, N., Peek, R., 1992. On stability and the worst imperfection shape in solids with nearly simultaneous eigenmodes. Int. J. Solids Struct. 29 (18), 2281–2299. doi:10.1016/0020-7683(92)90216-G.

Triantafyllidis, N., Schraad, M.W., 1998. Onset of failure in aluminum honeycombs under general in-plane loading. J. Mech. Phys. Solids 46 (6), 1089–1124.

Truesdell, C., Noll, W., (Editor), S.S.A., 2004. The Non-Linear Field Theories of Mechanics, third edition Springer-Verlag.

Truesdell, C.A., Toupin, R., 1960. The classical field theories. In: Flügge, S. (Ed.), Handbuch der Physik, vol. III/1. Springer-Verlag, pp. 226–793.

Vanderbauwhede, A., 1982. Local Bifurcation and Symmetry. Volume 75 of Research Notes in Mathematics, first edition, Pitman Publishing Inc.

Wohlever, J., Healey, T., 1995. A group theoretic approach to the global bifurcation analysis of an axially compressed cylindrical shell. Computer Methods in Applied Mechanics and Engineering 122 (3–4), 315–349. doi:10.1016/0045-7825(94)00734-5.